3D Reconstructions of Mouse Skeletal Muscle Reveal a Decrease in the MICOS Complex and Altered Mitochondrial Networks

Zer Vue[1*], Edgar Garza-Lopez[2*], Kit Neikirk[1*], Larry Vang[1], Heather Beasley[1], Amber Crabtree[1], Andrea G. Marshall[1], Sandra Murray[3], Antentor Hinton, Jr[1#]

[1] Department of Molecular Physiology and Biophysics, Vanderbilt University, Nashville, TN, 37232, USA.
[2] Department of Internal Medicine, University of Iowa, Iowa City, IA, 52242, USA.

*These authors share co-first authorship.
#These authors share senior authorship.

Corresponding Author:
Antentor Hinton
Department of Molecular Physiology and Biophysics
Vanderbilt University
antentor.o.hinton.jr@Vanderbilt.Edu 319-383-3095

Graphical Abstract:

ABSTRACT

Background: Skeletal muscle gradually loses mass, strength, endurance, and oxidative capacity during aging. Studies of bioenergetics and protein turnover show that mitochondria mediate this decline in function. Mitochondria cristae are essential for the production of ATP. While mitochondrial aging is associated with endoplasmic reticulum stress, fragmented mitochondria, and decreased mitochondrial capacity, the genes associated with morphological changes in mitochondria during aging still requires further elucidation Further, it is not completely understood how 3D mitochondrial networks and the specialization of mitochondria are altered during aging.

Methods: We measured changes in mitochondrial morphology and mitochondrial connectivity during the aging of the mouse gastrocnemius muscle through serial block facing-scanning electron microscopy and 3D reconstruction. Nanotunnels were also measured through 3D reconstruction. CRISPR/Cas9 KO was performed to examine changes in mitochondria upon loss of the mitochondrial contact site and cristae organizing system (MICOS) complex and optic atrophy 1 (OPA-1). Metabolomics were used to find key metabolite pathways changed upon off of the MICOS complex.

Results: We found changes in mitochondrial network configuration, nanotunneling, size, shape, number, contact sites, cristae organizing system (MICOS) dynamics and gene expression in skeletal muscle during aging. We also found an association of OPA-1 and the MICOS complex in the gastrocnemius with mitochondrial aging. Further, the loss of the MICOS complex was linked with decreased oxidative capacity, and altered mitochondrial metabolism.

Conclusions: To our knowledge, studies of mitochondrial changes in skeletal muscle throughout aging remains limited. 3D reconstructions of nanotunnels elucidated novel patterns of

mitochondrial aging in skeletal muscle. MICOS proteins decreased with age and mitochondrial morphology was similar between aged skeletal muscle and that of young mice with MICOS protein loss. In tandem, our data suggest a relationship between the MICOS complex and aging, which could be potentially linked to disease sates with additional 3D reconstruction.

Keywords: MICOS, aging, mitochondria, 3D morphometry; imaging; machine learning; mitochondrial disease; mitochondrion; nanotunnel; reconstruction; reticulum; serial block-face SEM; skeletal muscle.

INTRODUCTION

The loss of muscle mass associated with aging, known as sarcopenia, impacts the quality of life affecting both type I and type II fibers, but more so for type II fibers. The mitochondrial free radical theory of aging (MRFTA) proposes that the accumulation of reactive oxygen species (ROS) byproducts of mitochondrial respiration causes the aging damage [1–3]. The critical role of mitochondrial oxidative stress in aging has been shown using mitochondrial-targeted antioxidants, such as catalase targeted to mitochondria, in cardiac aging [4] and sarcopenia [5]. In addition to the main function of generating cellular ATP by oxidative phosphorylation [6], mitochondria play critical roles in ROS signaling, calcium homeostasis, programmed cell death, and regulation of innate immunity and stem cells. To carry out the tremendous variety of tasks, mitochondria maintain finely regulated ultrastructures, through various mechanisms, one of which is mitochondrial dynamic machinery through fission and fusion. Since their structure changes dynamically as mitochondria shift from fission to fusion. Important mitochondrial functions depend on the ultrastructure [7–9], it is important to examine mitochondrial structural changes over time. Essential mitochondrial functions are associated with the mitochondrial inner membrane folds known as cristae, which house the oxidative phosphorylation machinery[8] and various transporters. Our objective was to determine how aging alters mitochondrial networks and individual mitochondrial structures. We hypothesized that age-related oxidative stress causes increased mitochondrial mitophagy and fragmentation over time with concomitant losses in mitochondrial crista integrity.

Disruption of optic atrophy 1 (OPA-1), an inner membrane protein that regulates mitochondrial fusion, causes mitochondrial fragmentation and affects the dimensions, shapes, and sizes of the cristae [8]. Disruption of Drp1, a protein associated with mitochondrial fission, causes elongated mitochondria and resistance to remodeling of the cristae [10,11]. Nanotunnels or “mitochondria-on-a-string” are thin, double-membrane protrusions lacking cristae that allow mitochondria to communicate across distances. Nanotunnels may increase in mitochondrial disease [12,13] and may be associated with mitochondrial dysfunction during aging. Mutations in genes that regulate the morphology of cristae have been associated with aging cardiomyocytes [14]. These gene products are located at the crista junctions in the inner membrane and are a part of the mitochondrial contact site and cristae organizing system (MICOS), which are important for maintaining mitochondrial shape and size [15]. DRP1 or OPA-1 loss can similarly affect mitochondria morphology [16,17]. Cristae membranes contain the electron transport chain complexes and ATP synthase for ATP synthesis via oxidative phosphorylation [18–20]. Since mitochondrial morphology affects function, altering the structure by knocking out MICOS-

associated genes or the GTPase of OPA-1 could alter the metabolism and function of mitochondria during aging [18–20]. Critically, we predicted that MICOS-associated genes were lost over age, therefore, loss of MICOS-associated genes would mimic loss in mitochondria morphology observed across age.

To better understand the alterations of mitochondrial specialization ultrastructure in aging, we quantitatively analyzed 3D networks of specialized mitochondria at single-organelle resolution in skeletal muscle biopsies of mice at 3 months, 1 year, and 2 years of age. We compared size, shape, quantity, complexity, and branching of mitochondria using 3D reconstructions of aged gastrocnemius, and we measured nanotunneling in mouse muscles at these three ages. Multivariate analysis was used to identify changes in metabolites, the MICOS complex, OPA-1, nanotunneling, mitochondrial complexity, and morphological changes to better understand how mitochondrial specialization and structure change during aging.

RESULTS

Aging Results in Smaller, Shorter, Poorly Connected Mitochondria with Decreased Branching in Mouse Skeletal Muscle

The gastrocnemius is a mixed muscle with both oxidative fibers containing many mitochondria and glycolytic fibers with few mitochondria. This heterogeneity makes the gastrocnemius ideal to study changes in mitochondrial dynamics free radical theory of aging (MRFTA) proposes that the accumulation of reactive oxygen species (ROS) byproducts of mitochondrial respiration, such as hydroxyl radicals, causes damage that leads to aging [1–3]. Since many mitochondrial functions depend on structure [7–9], it is important to examine mitochondrial structural changes over time. We hypothesized that increasing mitochondrial mitophagy and fragmentation over time is concomitant with losses in mitochondrial crista integrity.

Our objective was to determine how aging alters mitochondrial networks and individual mitochondrial structure. We imaged gastrocnemius biopsies from young (3-month-old), mature (1-year-old) and aged (2-year-old) mice by serial block-face scanning electron microscopy (SBF-SEM) with resolutions of 10 µm for the x- and y- planes and 50 µm for the z-plane, which allows visualization of the electron connectome. IMF mitochondria are located between myofibrils, arranged in pairs at the z-band of each sarcomere, with 2D elongated tubular shapes [21]. However, it is not known how aging affects mitochondrial orientation, the structure of C-band sarcomeres, or the morphological changes in incomplete fission known as nanotunnels. For each region of interest across the three age groups, we analyzed 300 slices at 50 µm intervals at the transverse intervals. Approximately 50 IMF mitochondria were segmented from each image stack (Figure 1A-C) and a 3D surface view was generated (Figure 1A’’-C’’). We analyzed mitochondria sub-network volumes from four regions of interest with an average of 175 mitochondria for each mouse (n = 3), for a total of 500 mitochondria. Mitochondrial networks in aged mice showed largely interconnected mitochondria that were not composed of a single reticulum (Figures 1A’’’–C’’’). We found that mitochondrial volume decreased with age (Figures 1 A’’’–C’’) as did mitochondrial network volumes (Figure 1D). The area and perimeter of mitochondria of samples from 2-year-old mice were significantly lower than those from 3-month-old mice; however, there was no significant change for 1-year-old mice compared to 3-month-old mice (Figures 1E-F). While there was some variability across the three mice for each age cohort (SFigure 1), in general the trend showed a downwards trajectory emblematic of increased fragmentation and

smaller mitochondria. This showed that the size and length of mitochondria change with age, but the specific complexity of mitochondria, which is implicated with mitochondria communication, needed to be further elucidated.

We next measured mitochondrial complexity to better understand changes in mitochondrial shape during aged mitochondrial complexity, quantification of the 2D form factor as a 3D shape, using previously. We believed that less networks and simpler shape would occur as aging and dysfunction continued. Previously established methods [22,23] were used to determine three dimensional mitochondrial complexity from two dimensional form factor measurements. [22,23]. First, we first examined transverse (Figure 2A-C) and longitudinal (Figure 2A'-C') mitochondrial dimensions across ages in skeletal muscle. These measures showed networking and broad mitochondria. Mitochondrial branching index (MBI) is the ratio of transverse (Figures 2A–C) to longitudinal (Figures 2A'-C') branching, which better quantifies the orientation of the branching, and MCI and MBI together measure mitochondria morphology [22]. We found that MBI decreased across the age cohorts (Figure 2D). Since we observed in 3D reconstructions that mitochondrial populations are heterogeneous and diverse, we utilized mito-typing, which is the karyotype-like for arranging mitochondria [22], to capture the diversity of IMF mitochondria (Figure 2E). This analysis suggested at every volumetric measurement, mitochondria were smaller and less complex with age. We also measured sphericity to further understand changes in complexity. There was a progressive increase in sphericity with aging (Figure 2F). When examining the specific three male mice sampled for each age cohort, some variation exists for both metrics; however, the trends again clearly show sphericity stays consistent while MBI decreases across age (SFigure 2). Together, these measurements suggest that complexity decreases across all mitotypes with age.

Mitochondrial Nanotunnels Change in Size and Amount with Aging in Skeletal Muscle

To quantify nanotunnels in skeletal muscle, we performed 3D reconstruction in mice at three ages, measuring 550 mitochondria per mouse (n=3) using four different regions of interest. Although nanotunnels are reported to exist primarily in mitochondrial disease states [12], we found them in all three ages of mice (Figures 3A–C). The diversity and heterogeneity in the organization, sizing, and branching of nanotunnels necessitated mito-otyping (Figure 3D). We found nanotunnels in a greater proportion of mitochondria in 1-year-old mice than in 2-year-old mice (Figure 3E). However, the number of nanotunnels in each mitochondrion was significantly less in the 2-year-old mice than the 3-month-old and 1-year-old mice (Figure 3F). The length and diameter of nanotunnels increased in the older mice compared to the 3-month-old mice (Figures 3G–H), but the increase was significantly greater in the 1-year-old mice than the 2-year-old mice (Figures 3G–J). These data show that nanotunnel structure, frequency, and length change during aging.

Since mitochondrial dynamics and cristae change with aging (references), we measured transcripts for *Opa-1*, the gene associated with mitochondrial fusion, and *CHCHD3* (*Mic19*), *CHCHD6* (*Mic25*), and *Mitofilin* (*Mic60*), the genes for the principal MICOS complex subunits. We used reverse-transcriptase qPCR (RT-qPCR) to determine the effect of aging on transcription. Since aging causes fragmentation of mitochondria, a hallmark for loss of *Opa-1* and MICOS complex proteins, we hypothesized that aging would also lead to decreases in the associated MICOS complex proteins, as well as confirming prior studies which have found Opa-1 loss across aging [19,24–26]. We found progressive loss of both *Opa-1* and MICOS complex subunits, as measured by loss of transcripts for the proteins (Figure 4A–D). In 1- and 2-year-old

mice, the amount of mRNA made for the MICOS complex subunit genes or the *Opa-1* gene was less than half of that made in 3-month-old mice (Figures 4A–C). Furthermore, for all MICOS genes, there was a statistically significant decrease in the amount of mRNA over time with a higher level of significance in 2-year-old mice. These data suggest a correlation between mitochondrial morphologic changes and decreases in expression of genes for *Opa-1* and MICOS subunits *CHCHD3*, *CHCHD6*, and *Mitofilin* during aging; however, they are not sufficient to demonstrate causation, therefore we did additional to show that reduced protein expression levels may be responsible for the morphologic changes.

Changes in Cristae and Mitochondria in Myotubes and Oxygen Respiration Rate Upon Knockout of MICOS complex and *Opa-1*

From there, we saw the need to move to an in-vitro model to look at how the MICOS complex is implicated in mitochondria structure. The MICOS complex and OPA-1 are key players in mitochondrial biogenesis [15,19,27], but how their interactions regulate aging and mitochondrial superstructures is poorly understood. To determine the role of OPA-1 and the MICOS complex in mitochondrial structure and networking, we ablated the genes for *Opa-1* and the MICOS complex in isolated primary skeletal muscle cells from 3-month-old mice. We isolated primary satellite cells. From there, we differentiated myoblasts to myotubes. Using CRISPR/Cas9, guide RNA (Table 2), and a control plasmid, we transiently knockout the genes for MICOS complex components and *Opa-1* from skeletal muscle cells. As observed previously, in vitro deletion of OPA-1 altered mitochondrial morphology [16,28,29].
We measured 1250 mitochondria across 10 cells, using loss of *Opa-1* was a positive control for mitochondrial morphology changes. Although *Opa-1* expression decreases with age [30], the effect of the MICOS complex being lost in mitochondria morphology is unknown. Using transmission electron microscopy (TEM) images, we compared mitochondria and cristae in myotubes from wild type (WT) and knockouts of *Opa-1* and *Mitofilin* genes, which are essential for the organization of mitochondrial cristae [31,32] (Figures 5A–C). Mitochondrial average area decreased for both *Opa-1* and *Mitofilin* knockout myotubes (Figure 5D), while mitochondrial circularity (the roundness and symmetry of mitochondria) and number increased for both *Opa-1* and *Mitofilin* knockout myotubes (Figures 5E–F). For both *Opa-1* and *Mitofilin* knockouts, the number of cristae per mitochondrion decreased, as did the cristae score and cristae surface areas compared to the WT (Figures 5G–I). Cristae score measures the uniformity and regularity of cristae compared to typical cristae, with a lower number representing abnormality and dysfunction. We also compared WT with *Opa-1*, *CHCHD3*, and *CHCHD6* knockout myotubes (Figures 5P–S). Knockout of MICOS subunit *CHCHD3* results in fragmented mitochondria with less *Opa-1* as the cristae lose their normal structure [33]. Similarly, *CHCHD6* is important in maintaining crista structure and its downregulation results in hollow cristae lacking an electron-dense matrix, thereby inhibiting ATP production and cell growth [32,34,35]. Mitochondrial average area decreased for *Opa-1*, *CHCHD3*, and *CHCHD6* knockout myotubes (Figure 5T), while the circularity index and the number of mitochondria, once normalized, increased (Figures 5U–V). For *Opa-1*, *CHCHD3*, and *CHCHD6* knockouts, the number of cristae per mitochondrion decreased, as did the cristae score and cristae surface area compared to the WT (Figures 5W–Y). The least significant change was seen in the *CHCHD3* knockout. Together, these data show quantitative and structural changes in both mitochondria and cristae upon loss of MICOS proteins.

Loss of OPA-1 induces bioenergetic stress and decreased electron transport chain function [29] and ablation of the MICOS complex alters mitochondrial capacity [36,37]. We found that loss of OPA-1 or *Mitofilin* in myotubes decreased basal oxygen consumption rate (OCR) (Figures 5J–K) and decreased ATP-linked, maximum, and reserve capacity OCR (Figures 5L–N). Although OPA-1 knockout myotubes exhibited a decrease in proton leak, which represents protons that go from the mitochondria to matrix without producing ATP, *Mitofilin* knockouts showed no significant difference (Figure 5O). In *Opa-1*, *CHCHD3*, and *CHCHD6* knockouts, there was a decrease in basal, ATP-linked, maximum, and reserve capacity OCR compared to the control (Figures 5Z–AD). Although proton leak OCR decreased in *Opa-1* and *CHCHD3* knockout myotubes (Figure 5AE), there was no significant difference between the control and *CHCHD6*. The decrease in OCR may be attributed to smaller and fragmented mitochondria; mitochondrial density decreases as fragmentation targets them for autophagy [30,38]. Together, these results show that MICOS and *Opa-1* are essential for normal respiration of muscle tissue.

TEM provides mitochondrial detail, but not 3D morphology; therefore, we used SBF-SEM to look at the 3D structure of the mitochondria. Using myotubes with ablated genes for *Opa-1* and MICOS complex subunits, as described above, we measured a total of 200 mitochondria across 10 cells. We compared mitochondria in WT, *Opa-1* knockout, and *Mitofilin* knockout myotubes (Figures 6A–C) and found that compared to the elongated mitochondria in the WT, the 3D length was much shorter in *Opa-1* and *Mitofilin* knockouts (Figure 6D), and the volume of the mitochondria was less (Figure 6E). In similar experiments, we compared mitochondria in WT to those in *Opa-1*, *CHCHD3*, and *CHCHD6* knockout myotubes (Figures 6F–I) and found shorter mitochondria in the three knockout strains (Figure 6J). Similarly, the volume of mitochondria was also less in *CHCHD3*, *CHCHD6*, and *Opa-1* knockouts compared to the control (Figure 6K). The 3D reconstruction data, in combination with the prior TEM results, show how mitochondrial dynamics change with the loss of MICOS subunits.

Metabolomics Show Key Metabolite Changes in Knockout of MICOS Complex Proteins and *Opa-1* in Myotubes.

To determine the global effects of loss of *Opa-1* or the MICOS complex in skeletal muscle myotubes, we analyzed the metabolome to identify changes in metabolites that occurred with changes in mitochondria and cristae. Principal component analysis (PCA) revealed distinct populations in the control and the *Mitofilin* knockout strains, which suggested that their genotypes contributed to the clustering (Figure 7A). To identify metabolites with the most robust ability to discriminate between true positives and false positives, we constructed a model using analysis of variance (ANOVA) to determine several key metabolites that were statistically significant (Figure 7B). This unique metabolite signature revealed that *Mitofilin* plays a critical role in regulating amino acid metabolism and steroidogenesis (Figures 7C–D). Upregulation of steroidogenesis pathways may result from the increased fluidity of membranes caused by *Mitofilin* [39,40]. We also measured the effect of ablation of genes for *CHCHD3* and *CHCHD6* in skeletal muscle myotubes on bioenergetic metabolism. PCA revealed distinct populations in the control and the *CHCHD3* and CHCHD6 knockouts, which showed a similar profile (Figure 7E). We constructed a model using ANOVA to determine which metabolite changes in *CHCHD3* and *CHCHD6* knockouts were statistically significant (Figure 7F) There was a loss of protein synthesis and changes in carbohydrate metabolism (Figures 7G–H). Loss of *Opa-1* typically favors fatty acid synthesis, so these results showing increased carbohydrate metabolism differ from previous *Opa-1* knockout responses [41–43]. This atypical response was evident in the increase

in lactose and starch synthesis, but there was poor protein turnover, as seen in methionine metabolism (Figure 7H).

DISCUSSION

Mitochondrial morphology is linked to oxidative phosphorylation and the aging of mitochondria [6,7,22]. We produced high-resolution three-dimensional mitochondrial images and measured mitochondria in myotubes of skeletal muscles lacking components of the MICOS complex. We demonstrated that either aging or loss of MICOS proteins in skeletal muscle resulted in suboptimal mitochondria morphology, suggesting a correlation between aging and MICOS protein expression.

Previous studies using 3D focused ion beam-scanning electron microscopy (FIB-SEM) in human skeletal muscle [44] and in mouse muscle [45] characterized the networking of the mitochondria. Vincent et al. did quantitative 3D reconstructions using SBF-SEM to define the morphological differences in the skeletal muscles of humans versus mice, and they compared patients with primary mitochondrial DNA diseases with healthy controls [22]. Our 3D reconstruction of normal aged skeletal gastrocnemius muscle is a novel approach to study the connections between mitochondria and to determine how disconnections and reduced mitochondrial communication arising with age impact oxidative phosphorylation.

We studied skeletal muscle because it is affected by aging and highly mitochondrial dependent as well as mitochondria enriched. Mitochondria comprise ~6% of the cell volume in skeletal muscle [46]. Skeletal muscle has type I slow-twitch muscle fibers or type II fast-twitch muscle fibers; type I fibers are more effective for endurance, while type II fibers better support short bursts of muscle activity [46–48]. The morphologic data collected by our methods did not permit discrimination of the two fiber types, although we observed many variable muscle fibers within a sample and between all differently aged cohorts. In the future, it may be valuable for studies to distinguish fiber types; past studies in human skeletal muscle has done this by taking two portion of samples and assessing fiber type via sodium dodecyl sulfate-polyacrylamide gel electrophoresis [49].

Skeletal muscle may induce mitochondrial biogenesis by activating adenosine monophosphate-activate protein kinase (AMPK) [47]. As increased apoptosis, decreased regeneration rate, and reduced mobility happen across aging, decreased AMPK activity may explain the loss of skeletal muscle function [1,2,48]. Using 3D reconstructions, we found that all parameters of the mitochondria changed during aging including volume, area, and perimeter (Figure 1D-F), and the mitochondria became less interconnected. This increased fragmentation may be as a result of decreased mitochondrial fusion, as marked by decreases of OPA-1 across aging, which is a regulator of mitochondrial fusion. We also saw a decrease in the MBI during aging, which shows that mitochondria decrease in networking, but their shape may not radically change as they actually increase in sphericity as they age (Figure 2).

The change in morphology in aging mitochondria could be explained by the mitochondrial free radical theory of aging (MFRTA), which hypothesizes that the ROS byproducts of respiration result in hydroxyl radicals that damage every part of the body [1,2]. According to this theory, aerobic respiration and ATP production by mitochondria are ultimately responsible for aging through generation of ROS and its eventual accumulation of damage to mitochondria [2,50]. The MFRTA also proposes that ROS alter other functions of mitochondria, including ATP production, as they induce aging [50]. Since oxidative stress has been linked to

many diseases of aging (diabetes, heart disease, sarcopenia, arthritis, kidney disease) [51], specifically understanding the association between aging and mitochondria is important.

We found nanotunnels, which are thin, double-membrane mitochondrial connections that can transport proteins and nutrients, in all skeletal muscle samples. While healthy humans have almost no nanotunnels [22], we found a moderate number in "unaged" 3-month-old mice (Figures 3E–H), and a consistent increase of nanotunnels in the skeletal muscle of 1-year-old mice. This was unexpected and suggests that these structures may be having a beneficial role in skeletal muscle of mice. Given the association of nanotunnels with human disease, we predicted that the 2-year-old "aged" mouse skeletal muscle would have the most nanotunnels, however the nanotunnel number was quite heterogeneous in 2-year-old mice and less were observed [12,52]. The 2-year-old samples may have shown fewer nanotunnels as a consequence of the high rate of fragmentation (Figure 1) and lack of connectedness (Figure 2) preventing nanotunnel formation. In contrast, perhaps the remaining networks permitted the increased number of nanotunnels in 1-year moderately aged samples. The presence of nanotunnels in the healthy 3-month-old mouse skeletal muscle suggests significant differences in mouse versus human muscle [22].

MICOS proteins play key regulatory roles in mitochondrial structure and function [19,27,38]. We determined by TEM 3D reconstructions that the loss of *Mitofilin*, *CHCHD3*, and *CHCHD6* (Figures 5-6) resulted in fragmentation, disrupted cristae, and smaller mitochondria (Figures 5A–I, Figures 5P–Y; Figure 6), similar to the loss of OPA-1, which is known to cause changes in oxidative phosphorylation (Figures 5Z–AE) [19,24,29]. Overall, mitochondria lacking the MICOS genes had characteristics similar to those of aged mouse skeletal muscle (Figures 1−2). This similarity in phenotype suggests there may be an association. Thus, changes in mitochondrial morphology due to aging may be caused by a lack of MICOS gene expression. This is supported by the RT-qPCR data that showed decreased *CHCHD3*, *CHCHD6*, *Mitofilin*, and *Opa-1* transcription with aging (Figure 4). Although there is a link between aging and loss of *Opa-1* [25,30], little is known about the role of the MICOS complex in aging. Changes in mitochondrial architecture and loss of integrity may be caused by decreased MICOS proteins; thus, it will be important to develop methods to restore MICOS proteins and *Opa-1* lost during aging to decrease the deleterious effects of mitochondrial dysfunction. Although studies have examined the role of knockouts on mitochondrial dynamics, few studies have examined how loss of MICOS proteins may be restored to mitochondria [24,53].

Many studies have analyzed the mitochondrial metabolome using mouse skeletal muscles [46,54–58]. We found that loss of *Mitofilin* affected cristae morphology (Figures 6G–I), decreased oxidative phosphorylation (Figure 5J), and may have increased lipid and steroid synthesis, which may be important for mitochondrial endoplasmic reticulum contact (MERC) regulation and cristae formation. We found an increase in tryptophan and methyl histidine metabolism (Figure 6D) and an increase in taurine metabolism and hypotaurine, a key sulfur-containing amino acid for the metabolism of fats. Loss of *Opa-1* also changes amino acid and lipid metabolism, similar to the loss of *Mitofilin* [41–43]. Steroidogenesis, which makes the membrane less rigid, was increased. Since the loss of *Mitofilin*, *CHCHD6*, or *CHCHD3* caused a loss of oxidative capacity (Figure 5), increased steroid synthesis may allow the cell to recover bioenergetic functions, as steroid compounds decrease membrane viscosity, with the incorporation of estrogen [39]. In the absence of *Mitofilin*, the cristae junctions and contact sites fall apart [59]; thus, *Mitofilin* is critical for maintaining cristae [60,61]. Cells lacking *Mitofilin* may make steroids to help the membrane to reconfigure broken cristae. Since the loss of *Opa-1* causes more MERCs [3], loss of *Mitofilin* may increase phospholipids (Figure 7D) because of increased smooth MERCs, which are associated

with lipid changes [62]. This is supported by the fact that biosynthesis of phosphatidylethanolamine and phosphatidylcholine and metabolism of arachidonic acid and sphingolipid increased with loss of *Mitofilin* (Figure 7D). Since these phospholipids aggregate around MERCs and may shuffle into the endoplasmic reticulum (ER), *Mitofilin* may be a critical gene for regulating cristae morphology and with a key role in regulating mitochondrial metabolism, which is novel.

Mitofilin may be a an important target in the future. Loss of *Mitofilin* may lead to ER stress, which, via ATF4, activates amino acid transporters [63] that further activate mTORC1. ER stress activates mTORC as a result of a decrease in glucose [58]. Critically, mTORC1 affects glucose homeostasis [64], and this may lead to inefficiency in energy use. This can result in changes in autophagy. Therefore, as a downstream effect of *Mitofilin* loss increasing mTORC1, this may explain why deletion of MICOS in *Drosophila* increases autophagy [38]. Similarly, previously loss of *Opa-1* increases ER stress [29], and loss of *Mitofilin* may cause a similar increase in amino acid catabolism. If ER stress activates amino acid transporters, branched-chain amino acids could increase ER stress, resulting in a positive feedback loop that affects the health of the cell, cellular energy, metabolism, and antioxidants. ER stress may also be responsible for the poor performance and fragmentation of mitochondria (Figure 5). Loss of *Mitofilin* may result in the breakdown of protein pathways that regulate ER stress. Other amino acid pathways, such as homocysteine (Figure 7D), are involved in triglyceride uptake and increased intracellular cholesterol, suggesting that proteins like ATF4 [58] and the MICOS complex [15,27] are important for aging. In particular, the MICOS components may prevent mitochondrial fragmentation by blocking ER stress pathways in aging. Further studies are needed to better understand the role of MICOS in MERC formation and the relation between smooth MERC and lipid synthesis.

Although *Mitofilin* is a key component of the MICOS complex, other components are likely also important. Mic10 has a role beyond organizing cristae by also binding to ATP synthase, independent of oligomerization, to support respiration and metabolic adaptation [65]. The loss of *CHCHD3* or *CHCHD6* leads to a decrease in and disassembly of all *Mitofilin* subcomplex components in mammals, with abnormal cristae morphology and growth defects [34,66–71]. Downregulation of *CHCHD3* is linked to type 2 diabetes [72]. In our metabolomics enrichment dataset (Figure 7H), loss of *CHCHD3* or *CHCHD6* in mouse myotubes resulted in a preference for alternative fuel sources, such as lactate, lactose, and starches. Supplementation of healthy myotubes with galactose leads to a 30% increase in oxidative capacity (i.e., OCR) due to an increase in AMPK phosphorylation and cytochrome c oxidase (COX) activity, thereby forcing cells to become more oxidative to maintain ATP levels [73]. In our samples, as oxidative metabolism decreased, anaerobic metabolism and lactate levels increased, forcing cells to produce ATP by anaerobic glycolysis. However, long and high-level exposure to D-galactose generates free radicals, which alter MERCs, cause mitochondrial dysfunction, and induce aging [2,74]. This is the likely explanation for mitochondrial fragmentation in aged samples and loss of the MICOS complex, which should be investigated further.

In conclusion, we present a quantitative evaluation of mitochondrial and cristae morphology in mouse skeletal muscle using 3D reconstructions and TEM analysis. We found oxidative differences upon loss of MICOS proteins. 3D reconstructions of nanotunnels in mitochondria showed novel patterns with a moderate number of nanotunnels in young skeletal mouse tissue and relatively low numbers in the most aged mouse skeletal muscles. Similar changes in mitochondrial morphology were observed in aging muscles and for loss of MICOS proteins in mouse skeletal muscle, and MICOS proteins decreased with age. This suggests a relationship between the MICOS complex and aging, and further studies through 3D

reconstruction could elucidate the linkage between age-related muscle dysfunction, the MICOS complex, and disease states in mitochondria.

EXPERIMENTAL PROCEDURES

Animal Care and Maintenance

All procedures for the care of mice were in accordance with humane and ethical protocols approved by the University of Iowa Animal Care and Use Committee (IACUC) following the National Institute of Health Guide for the Care and Use of Laboratory Animals as described previously [29]. All experiments used WT male C57Bl/6J mice housed at 22°C on a 12-hour light, 12-hour dark cycle with free access to water and standard chow. Mice were anesthetized with 5% isoflurane/95% oxygen.

RNA Extraction and RT-qPCR

Total RNA was extracted from tissue using TRIzol reagent (Invitrogen), purified with the RNeasy kit (Qiagen Inc), and quantitated by the absorbance at 260 nm and 280 nm using a NanoDrop 1000 (NanoDrop products, Wilmington, DE, USA) spectrophotometer. Total RNA (~1 µg) was reverse-transcribed using a High-Capacity cDNA Reverse Transcription Kit (Applied Biosciences, Carlsbad CA) followed by real-time quantitative PCR (qPCR) reactions using SYBR Green (Life Technologies, Carlsbad, CA) [75]. Triplicate samples for qPCR (~50 ng) in a 384-well plate were placed into ABI Prism 7900HT instrument (Applied Biosystems) programmed as follows: 1 cycle at 95°C for 10 min; 40 cycles of 95°C for 15 s; 59°C for 15 s, 72°C for 30 s, and 78°C for 10 s; 1 cycle of 95°C for 15 s; 1 cycle of 60°C for 15 s; and one cycle of 95°C for 15 s. Data were normalized to glyceraldehyde-3-phosphate dehydrogenase (*GAPDH*), and results are shown as fold changes. qPCR primers were designed using Primer-Blast or were previously published sequences [29] as shown in Table 1.

Table 1: qPCR Primers Used

Gene	Primers	
Opa-1	Forward	5’-ACCAGGAGACTGTGTCAA-3’
	Reverse	5’-TCTTCAAATAAACGCAGAGGTG-3’
CHCHD3	Forward	5’-GAAAAGAATCCAGGCCCTTCCACGCGC-3’
	Reverse	5’-CAGTGCCTAGCACTTGGCACAACCAGGAA-3’
CHCHD6	Forward	5’-CTCAGCATGGACCTGGTAGGCACTGGGC-3’
	Reverse	5’-GCCTCAATTCCCACATGGAGAAAGTGGC-3’
Mitofilin	Forward	5’-CCTCCGGCAGTGTTCACCTAGTAACCCCTT-3’
	Reverse	5’-TCGCCCGTCGACCTTCAGCACTGAAAACCTAT-3’

Isolation of Satellite Cells

Satellite cell differentiation was performed as previously described with slight modifications [16,29]. Gastrocnemius muscles were dissected from 8−10 week- old WT mice and washed twice with 1× PBS supplemented with 1% penicillin-streptomycin and Fungizone (300 mL/100 mL). DMEM-F12 medium with collagenase II (2 mg/mL), 1% penicillin-streptomycin, and Fungizone (300 mL/100 mL) was added to the muscle which was agitated for 90 min at 37°C. For the second wash, collagenase II was changed to 0.5 mg/mL, and the muscle was agitated for 30 min at 37°C. The tissue was cut, passed through a 70 mm cell strainer, and after centrifugation satellite cells were plated on BD Matrigel-coated dishes. To differentiate cells into myoblasts, a mixture of DMEM-F12, 20% fetal bovine serum (FBS), 40 ng/mL basic fibroblast growth factor

(bFGF, R and D Systems, 233-FB/CF), 1× non-essential amino acids, 0.14 mM β-mercaptoethanol, and 1× penicillin/streptomycin, and Fungizone was used. Myoblasts were maintained with 10 ng/mL bFGF and when cells reached 80% confluence, myoblasts were differentiated in DMEM-F12, 2% FBS, 1× insulin–transferrin–selenium medium. Cells were cultured at 37°C, 5% CO_2 Dulbecco's modified Eagle's medium (DMEM; GIBCO) supplemented with 10% FBS (Atlanta Bio selected), and 1% penicillin-streptomycin (Gibco, Waltham, MA, USA).

CRISPR-Cas9 Knockouts

After three days, myotubes were infected with adenovirus to produce the following knockouts—control CRISPR/Cas9 (sc-418922), *CHCHD6* (Mic25) CRISPR (sc-425817), *CHCHD3* (Mic19) CRISPR (sc-425804), and *mitofilin* (Mic60) CRISPR (sc-429376) (Santa Cruz Biotechnology, California, US), with the use of guide RNA (Table 2). We incubated 2.5% relevant CRISPR, 2.5% RNAiMax (ThermoFisher Scientific; 13778075), and 95% Opti-MEM (Gibco; 31985070) in a tube for 20 minutes. Cells were washed twice with PBS after removal of the medium and 800 µl of OPT-MEM and 200 µL of the CRISPR mixture were added to each well, ran in triplicates. Cells were incubated for 4 hours at 37 C, 1.0 mL of DMEM medium was added, cells were incubated overnight The myotubes were then washed with PBS and the medium was replaced. Experiments were performed between 3 and 7 days after infection for a total of 6 days of differentiation.

Table 2: Guide RNA and Plasmids Used

Gene Name	Type of Plasmid	CAS Number
Mitofilin	CRISPR/Cas9 KO (m)	sc-429376
CHCHD6	CRISPR/Cas9 KO (m)	sc-425817
CHCHD3	CRISPR/Cas9 KO (m)	sc-425804
Control	CRISPR/Cas9 KO (m)	sc-418922

Serial Block-Face Scanning Electron Microscope (SBF-SEM) Processing of Mouse Muscle Fibers

SBF-SEM was performed as described previously [17,28,76]. Male mice were anesthetized with 5% isoflurane. Once the hair and skin were removed, the hindlimbs were incubated in 2% glutaraldehyde with 100 mM phosphate buffer for 30 min. Gastrocnemius muscles were dissected, cut into 1-mm^3 cubes, and incubated in 2.5% glutaraldehyde, 1% paraformaldehyde, 120 mM sodium cacodylate solution for 1 hour. Tissues were washed three times with 100 mM cacodylate buffer at room temperature before immersion in 3% potassium ferrocyanide and 2% osmium tetroxide for 1 hour at 4°C, then treated with 0.1% thiocarbohydrazide, 2% filtered osmium tetroxide for 30 min, and left overnight in 1% uranyl acetate at 4°C. Between each step, three de-ionized water washes were performed. The following day, samples were immersed in 0.6% lead aspartate solution for 30 min at 60°C and dehydrated in graded concentrations of acetone. Dehydration was for five min each in 20%, 50%, 70%, 90%, 95%, and 100% acetone.Tissues were impregnated in Epoxy Taab 812 hard resin, then embedded in fresh resin, and polymerized at 60°C for 36–48 hours. Once polymerization was complete, blocks were sectioned for TEM to identify areas of interest, trimmed to 0.5 mm × 0.5 mm, and glued to aluminum pins. Afterward, pins were placed in an FEI/Thermo Scientific Volumescope 2 SEM, a state-of-the-art SBF imaging system. We obtained 300−400 ultrathin (0.09 µm) serial sections

from the blocks that were processed for conventional TEM. All sections were collected onto formvar-coated slot grids (Pella, Redding CA), stained, and imaged as previously described [17,28,76].

Quantification of TEM Micrographs and Parameters Using ImageJ

Quantification of TEM images was performed as described previously using the National Institutes of Health (NIH) *ImageJ* software [16,28]. Cells were divided into four quadrants and two quadrants were selected randomly for complete analysis. From each individual, a minimum of 10 cells were measured with three analyses to obtain accurate and reproducible values. If variability occurred, the number of cells was expanded to 30 cells per individual to reduce the variability.

Segmentation and Quantification of 3D SBF-SEM Images Using Amira

For 3D reconstruction, SBF-SEM images were manually segmented in Amira as described previously [17,28]. All serial sections (300−400 slices) were loaded onto Amira and structural features were traced manually on sequential slices of micrograph blocks. Structures in mice were collected from 30–50 serial sections that were then stacked, aligned, and visualized using Amira to make videos and quantify volumetric structures. An average of 500 total mitochondria across four regions of interest from 3 mice were collected for quantification. For 3D reconstruction of myotubes, approximately 20 mitochondria from a minimum of 10 cells were collected. Quantification of SBF-SEM images was performed as described previously [17] using the Amira software (Thermo Scientific). Many parameters were automatically measured by Amira. For useful metrics that are not automated, algorithms for those measurements were entered manually.

Data Analysis

All SBF-SEM and TEM data were presented as the mean of at least three independent experiments with similar outcomes. Results were presented as mean ± standard error with individual data points shown. Data with only two groups were analyzed using an unpaired, t-test. For nanotunnel quantification, a Mann-Whitney test (unpaired, nonparametric) t-test was performed between two groups. If more than two groups were compared, one-way ANOVA was performed, and significance was assessed using Fisher's protected least significant difference (LSD) test. GraphPad Prism software package was used for t-tests and ANOVA analyses (La Jolla, CA, USA). For all statistical analyses, $p < 0.05$ indicated a significant difference. Higher degrees of statistical significance (**, ***, ****) were defined as $p < 0.01$, $p < 0.001$, and $p < 0.0001$, respectively.

Gas Chromatography-Mass Spectrometry (GC-MS)

Samples were extracted for metabolites in −80°C 2:2:1 methanol/acetonitrile/water that contained a mixture of nine internal standards (d_4-citric acid, $^{13}C_5$-glutamine, $^{13}C_5$-glutamic acid, $^{13}C_6$-lysine, $^{13}C_5$-methionine, $^{13}C_3$-serine, d_4-succinic acid, $^{13}C_{11}$-tryptophan, d_8-valine; Cambridge Isotope Laboratories) at a concentration of 1 µg/mL each, at a ratio of 18:1 (extraction solvent:sample volume). Cells were lyophilized overnight before extraction and homogenized with a ceramic bead mill homogenizer after the addition of extraction buffer. Samples were incubated for one hour at −20°C and centrifuged at maximum speed for 10 min. All supernatants were transferred to fresh tubes and pooled quality control (QC) samples were prepared by adding an equal volume of each sample to a fresh 1.5 mL microcentrifuge tube. A speed vac was used to evaporate the pooled QCs, samples, and processing blanks, which were

made by adding extraction solvent to microcentrifuge tubes. Derivatives of the dried products were obtained using methoxamine hydrochloride (MOX) and *N*,O-bis(trimethylsilyl)trifluoroacetamide (TMS). Products were rehydrated in 30 µL of 11.4 mg/mL Molybdenum Carbide (MOC) in anhydrous pyridine (VWR), vortexed for 10 minutes, and incubated at 60°C for 1 hour. Then 20 µL of TMS was added, vortexing was repeated for one min, and samples were heated for an hour at 60°C. Samples of 1 µL were analyzed by GC-MS using a Thermo Trace 1300 GC with a TraceGold TG-5SilMS column for GC chromatographic separation. The GC temperature was set at 250°C for the inlet, with the oven temperature at a gradient with 3 min at 80 °C, increasing by 20°C a minute to a final 280°C for the last 8 minutes. The settings for the GC machine were 20:1 split ratio, split flow; 24 µL/min, purge flow; 5 mL/min, carrier mode; constant flow, carrier flow rate: 1.2 mL/min. Between each injection sample, the column was washed three times with pyridine. Metabolites were detected using the Thermo ISQ single quadrupole mass spectrometer, with data acquired from 3.90 to 21.00 min in the EI mode (70 eV) by single-ion monitoring. The profiling of the metabolites was performed using TraceFinder 4.1 with standard verified peaks and retention times. TraceFinder was used to compare metabolite peaks in each sample against an in-house library of standards. For these standards, retention times and fragment ions for each were analyzed, with fragment ions for both the target peak and two confirming ions. For the samples, we identified metabolites that matched both retention times and the three fragment ions. TraceFinder was also used for GC-MS peak integration to obtain peak areas for each metabolite. After this analysis, we used previously described protocols [77] to correct for drift over time by using QC samples run at both the beginning and end of the sequence. The data was then normalized to an internal standard to control for extraction, derivatization, and/or loading effects.

Liquid Chromatography-Mass Spectrometry (LC-MS)

Myotubes were dried, rehydrated in 40 µL acetonitrile:water (1:1), and vortexed. For LC-MS, 2 µL of the sample was used with a Thermo Q Exactive hybrid quadrupole Orbitrap mass spectrometer with a Vanquish Flex UHPLC system and a Millipore SeQuant ZIC-pHILIC column (length area = 2.1 × 150 mm, 5 µm particle size) with a ZIC-pHILIC guard column (length area = 20 × 2.1 mm). The mobile phase comprised solvent A (20 mM ammonium carbonate [$(NH_4)_2CO_3$] and 0.1% ammonium hydroxide [NH_4OH]) and solvent B (acetonitrile). The mobile phase gradient started at 80% solvent B, decreased to 20% solvent B over 20 min, returned to 80% solvent B in 0.5 min, and was held at 80% for 7 min [78]. From there, the mass spectrometer was operated in the full-scan, polarity-switching mode for 1 to 20 min, spray voltage set to 3.0 kV, capillary heated at 275°C, and HESI probe heated at 350°C. The sheath gas flow, auxiliary gas flow, and sweep gas flow were 40 units, 15 units, and 1 unit, respectively. We examined an *m*/*z* range of 70–1000, the resolution was set at 70,000, the AGC target at 1×10^6, and the maximum injection time was set to 200 ms [77].

TraceFinder 4.1 software was used for analysis and metabolites were identified based on an in-house library. Drift was corrected for as described above [77]. Data were normalized and further visualization and analysis were performed on MetaboAnalyst 5.0 [79].

Analyzing Metabolomic Data

Metabolomic analysis was performed as described previously [80] using a web service called MetaboAnalyst 5.0 (https://www.metaboanalyst.ca/MetaboAnalyst/ModuleView.xhtml, last accessed on 8 February 2022) that combines machine learning methods and statistics to group

data using PCA, heat mapping, metabolite set enrichment analysis, and statistical analysis. One-way ANOVA and Fisher's LSD multiple comparison test were also used. PCA uses score plots to provide an overview of variance for the principal components. Heatmaps separate hierarchical clusters leading to progressively larger clusters. Clusters are based on similarity using Euclidean distance and Ward's linkage to minimize the clustering needed. Metabolite Set Enrichment Analysis (MSEA), which determines whether a set of functionally related metabolites is altered, can be used to identify consistent changes across many metabolites with similar roles. Overrepresentation analysis determines whether a group of compounds is overrepresented in comparison to pure chance and whether a group of metabolites have similar changes. In this analysis, the fold enrichment was calculated by dividing the observed hits by the expected metabolites. Expected number of hits are calculated by MetaboAnalyst 5.0. GraphPad Prism software (La Jolla, CA, USA) was used for statistical analysis with data expressed as mean ± standard deviation, and one-tailed p-values ≤ 0.01 were considered significant.

Measurement of OCR Using Seahorse

To measure cellular respiration, the XF24 extracellular flux (XF) bioanalyzer (Agilent Technologies/Seahorse Bioscience, North Billerica, MA, USA) was used. Cells were plated at a density of 2×10^4 per well and differentiated. After 3 days of differentiation, *Opa-1*, *CHCHD3*, *CHCHD6*, or *Mitofilin* genes were knocked down as described above. Three days after knockout, the medium was changed to XF-DMEM, and cells were kept in a non-CO_2 incubator for 60 min. The basal OCR was measured in XF-DMEM. Oxygen consumption was also measured after the addition of oligomycin (1 μg/mL), carbonyl cyanide 4-(trifluoromethoxy)phenylhydrazone (FCCP; 1 μM), rotenone (1 μM), or antimycin A (10 μM) [81]. Cells were then switched to glucose-free XF-DMEM and kept in a non-CO_2 incubator for 60 min for the glycolysis stress test. Seahorse experimental data are for triplicate Seahorse plates. Three independent experiments were performed with four to six replicates for each time and for each condition and representative data from the replicates are shown.

NOVELTY AND SIGNIFICANCE

It is known that aging causes fragmentation and alters mitochondria dysfunction. However, we have further expanded upon these results in several ways. We have examined the specific structural changes across aging in mitochondria. We are also the first to examined changes in nanotunnel structure, specifically using 3D reconstruction, across aging. We have found an MICOS complex implication for protection of mitochondria morphology protection against aging. We are novel for using SBF-SEM volume scope and 3D reconstruction to describe fine details in mitochondria morphology across both aging and loss of MICOS complex. We are furthermore the first to examine nanotunnels in skeletal muscle and use 3D reconstruction.

ACKNOWLEDGEMENTS

We would like to thank Melanie McReynolds for her advice on processing metabolomic samples and Mariya Sweetwyne for her advice as an aging expert.

FUNDING

This work was supported by UNCF/BMS EE United Negro College Fund/Bristol-Myers Squibb E.E. T-32, number DK007563 entitled Multidisciplinary Training in Molecular Endocrinology to

Z.V.; Just Postgraduate Fellowship in the Life Sciences Fellowship to H.K.B.; NSF MCB #2011577I to S.A.M.; The United Negro College Fund/Bristol-Myers Squibb E.E. Just Faculty Fund, Burroughs Wellcome Fund Career Awards at the Scientific Interface Award, Burroughs Wellcome Fund Ad-hoc Award, National Institutes of Health Small Research Pilot Subaward to 5R25HL106365-12 from the National Institutes of Health PRIDE Program, DK020593, Vanderbilt Diabetes and Research Training Center for DRTC Alzheimer's Disease Pilot & Feasibility Program to A.H.J. Its contents are solely the responsibility of the authors and do not necessarily represent the official view of the NIH. The funders had no role in study design, data collection and analysis, decision to publish, or preparation of the manuscript.

CONFLICT OF INTEREST

The authors declare that they have no conflict of interest.

REFERENCES

1. Bratic A, Larsson N-G. The role of mitochondria in aging. *The Journal of clinical investigation*. 2013;123:951–957.

2. Barja G. The mitochondrial free radical theory of aging. *Progress in molecular biology and translational science*. 2014;127:1–27.

3. Rowland AA, Voeltz GK. Endoplasmic reticulum–mitochondria contacts: function of the junction. *Nature reviews Molecular cell biology*. 2012;13:607–615.

4. Dai D-F, Santana LF, Vermulst M, Tomazela DM, Emond MJ, MacCoss MJ, Gollahon K, Martin GM, Loeb LA, Ladiges WC, Rabinovitch PS. Overexpression of catalase targeted to mitochondria attenuates murine cardiac aging. *Circulation*. 2009;119:2789–2797.

5. Xu H, Ranjit R, Richardson A, Van Remmen H. Muscle mitochondrial catalase expression prevents neuromuscular junction disruption, atrophy, and weakness in a mouse model of accelerated sarcopenia. *J Cachexia Sarcopenia Muscle*. 2021;12:1582–1596.

6. Friederich M, Hansell P, Palm F. Diabetes, oxidative stress, nitric oxide and mitochondria function. *Current diabetes reviews*. 2009;5:120–144.

7. Renken CW. The structure of mitochondria. 2004.

8. Cogliati S, Enriquez JA, Scorrano L. Mitochondrial cristae: where beauty meets functionality. *Trends in biochemical sciences*. 2016;41:261–273.

9. Kühlbrandt W. Structure and function of mitochondrial membrane protein complexes. *BMC biology*. 2015;13:1–11.

10. Otera H, Ishihara N, Mihara K. New insights into the function and regulation of mitochondrial fission. *Biochimica et Biophysica Acta (BBA)-Molecular Cell Research*. 2013;1833:1256–1268.

11. Favaro G, Romanello V, Varanita T, Desbats MA, Morbidoni V, Tezze C, Albiero M, Canato M, Gherardi G, De Stefani D. DRP1-mediated mitochondrial shape controls calcium homeostasis and muscle mass. *Nature communications*. 2019;10:1–17.

12. Vincent AE, Turnbull DM, Eisner V, Hajnóczky G, Picard M. Mitochondrial Nanotunnels. *Trends Cell Biol*. 2017;27:787–799.

13. Zhang L, Trushin S, Christensen TA, Bachmeier BV, Gateno B, Schroeder A, Yao J, Itoh K, Sesaki H, Poon WW. Altered brain energetics induces mitochondrial fission arrest in Alzheimer's Disease. *Scientific reports*. 2016;6:1–12.

14. Zhang J, He Z, Fedorova J, Logan C, Bates L, Davitt K, Le V, Murphy J, Li M, Wang M, Lakatta EG, Ren D, Li J. Alterations in mitochondrial dynamics with age-related Sirtuin1/Sirtuin3 deficiency impair cardiomyocyte contractility. *Aging Cell*. 2021;20:e13419.

15. Kozjak-Pavlovic V. The MICOS complex of human mitochondria. *Cell and tissue research*. 2017;367:83–93.

16. Lam J, Katti P, Biete M, Mungai M, AshShareef S, Neikirk K, Lopez EG, Vue Z, Christensen TA, Beasley HK. A Universal Approach to Analyzing Transmission Electron Microscopy with ImageJ. *bioRxiv*. 2021.

17. Garza-Lopez E, Vue Z, Katti P, Neikirk K, Biete M, Lam J, Beasley HK, Marshall AG, Rodman TA, Christensen TA, Salisbury JL, Vang L, Mungai M, AshShareef S, Murray SA, Shao J, Streeter J, Glancy B, Pereira RO, Abel ED, Hinton A. Protocols for Generating Surfaces and Measuring 3D Organelle Morphology Using Amira. *Cells*. 2022;11:65.

18. Rampelt H, Zerbes RM, van der Laan M, Pfanner N. Role of the mitochondrial contact site and cristae organizing system in membrane architecture and dynamics. *Biochimica et Biophysica Acta (BBA)-Molecular Cell Research*. 2017;1864:737–746.

19. Hu C, Shu L, Huang X, Yu J, Gong L, Yang M, Wu Z, Gao Z, Zhao Y, Chen L. OPA1 and MICOS Regulate mitochondrial crista dynamics and formation. *Cell death & disease*. 2020;11:1–17.

20. Friedman JR, Mourier A, Yamada J, McCaffery JM, Nunnari J. MICOS coordinates with respiratory complexes and lipids to establish mitochondrial inner membrane architecture. *Elife*. 2015;4:e07739.

21. Vendelin M, Béraud N, Guerrero K, Andrienko T, Kuznetsov AV, Olivares J, Kay L, Saks VA. Mitochondrial regular arrangement in muscle cells: a "crystal-like" pattern. *American Journal of Physiology-Cell Physiology*. 2005;288:C757–C767.

22. Vincent AE, White K, Davey T, Philips J, Ogden RT, Lawless C, Warren C, Hall MG, Ng YS, Falkous G. Quantitative 3D mapping of the human skeletal muscle mitochondrial network. *Cell reports*. 2019;26:996–1009.

23. Koopman WJH, Visch H-J, Verkaart S, van den Heuvel LWPJ, Smeitink JAM, Willems PHGM. Mitochondrial network complexity and pathological decrease in complex I activity are tightly correlated in isolated human complex I deficiency. *Am J Physiol Cell Physiol*. 2005;289:C881-890.

24. Zheng J, Croteau DL, Bohr VA, Akbari M. Diminished OPA1 expression and impaired mitochondrial morphology and homeostasis in Aprataxin-deficient cells. *Nucleic acids research*. 2019;47:4086–4110.

25. Varanita T, Soriano ME, Romanello V, Zaglia T, Quintana-Cabrera R, Semenzato M, Menabò R, Costa V, Civiletto G, Pesce P. The OPA1-dependent mitochondrial cristae remodeling pathway controls atrophic, apoptotic, and ischemic tissue damage. *Cell metabolism*. 2015;21:834–844.

26. Khin PP, Hong Y, Yeon M, Lee DH, Lee JH, Jun H-S. Dulaglutide improves muscle function by attenuating inflammation through OPA-1-TLR-9 signaling in aged mice. *Aging (Albany NY)*. 2021;13:21962–21974.

27. Li H, Ruan Y, Zhang K, Jian F, Hu C, Miao L, Gong L, Sun L, Zhang X, Chen S. Mic60/Mitofilin determines MICOS assembly essential for mitochondrial dynamics and mtDNA nucleoid organization. *Cell Death & Differentiation*. 2016;23:380–392.

28. Hinton A, Katti P, Christensen TA, Mungai M, Shao J, Zhang L, Trushin S, Alghanem A, Jaspersen A, Geroux RE. A comprehensive approach for artifact-free sample preparation and assessment of mitochondrial morphology in tissue and cultured cells. *bioRxiv*. 2021.

29. Pereira RO, Tadinada SM, Zasadny FM, Oliveira KJ, Pires KMP, Olvera A, Jeffers J, Souvenir R, Mcglauflin R, Seei A. OPA 1 deficiency promotes secretion of FGF 21 from muscle that prevents obesity and insulin resistance. *The EMBO journal*. 2017;36:2126–2145.

30. Tezze C, Romanello V, Desbats MA, Fadini GP, Albiero M, Favaro G, Ciciliot S, Soriano ME, Morbidoni V, Cerqua C, Loefler S, Kern H, Franceschi C, Salvioli S, Conte M, Blaauw B, Zampieri S, Salviati L, Scorrano L, Sandri M. Age-Associated Loss of OPA1 in Muscle Impacts Muscle Mass, Metabolic Homeostasis, Systemic Inflammation, and Epithelial Senescence. *Cell Metab*. 2017;25:1374-1389.e6.

31. John GB, Shang Y, Li L, Renken C, Mannella CA, Selker JM, Rangell L, Bennett MJ, Zha J. The mitochondrial inner membrane protein mitofilin controls cristae morphology. *Molecular biology of the cell*. 2005;16:1543–1554.

32. Ding C, Wu Z, Huang L, Wang Y, Xue J, Chen S, Deng Z, Wang L, Song Z, Chen S. Mitofilin and CHCHD6 physically interact with Sam50 to sustain cristae structure. *Scientific reports*. 2015;5:1–11.

33. Darshi M, Taylor SS. Mitochondrial ChChD3 acts as a Scaffold for Mitofilin, Sam50 and PKA. 2008.

34. An J, Shi J, He Q, Lui K, Liu Y, Huang Y, Sheikh MS. CHCM1/CHCHD6, novel mitochondrial protein linked to regulation of mitofilin and mitochondrial cristae morphology. *Journal of Biological Chemistry*. 2012;287:7411–7426.

35. Ott C, Dorsch E, Fraunholz M, Straub S, Kozjak-Pavlovic V. Detailed analysis of the human mitochondrial contact site complex indicate a hierarchy of subunits. *PloS one*. 2015;10:e0120213.

36. Kondadi AK, Anand R, Reichert AS. Functional interplay between cristae biogenesis, mitochondrial dynamics and mitochondrial DNA integrity. *International journal of molecular sciences*. 2019;20:4311.

37. Stephan T, Brüser C, Deckers M, Steyer AM, Balzarotti F, Barbot M, Behr TS, Heim G, Hübner W, Ilgen P. MICOS assembly controls mitochondrial inner membrane remodeling and crista junction redistribution to mediate cristae formation. *The EMBO journal*. 2020;39:e104105.

38. Wang L, Hsu T, Lin H, Fu C. Drosophila MICOS knockdown impairs mitochondrial structure and function and promotes mitophagy in muscle tissue. *Biology Open*. 2020;9:bio054262.

39. Torres MJ, Kew KA, Ryan TE, Pennington ER, Lin C-T, Buddo KA, Fix AM, Smith CA, Gilliam LA, Karvinen S, Lowe DA, Spangenburg EE, Zeczycki TN, Shaikh SR, Neufer PD. 17β-Estradiol Directly Lowers Mitochondrial Membrane Microviscosity and Improves Bioenergetic Function in Skeletal Muscle. *Cell Metabolism*. 2018;27:167-179.e7.

40. Kitajima Y, Ono Y. Estrogens maintain skeletal muscle and satellite cell functions. *Journal of Endocrinology*. 2016;229:267–275.

41. Wasilewski M, Semenzato M, Rafelski SM, Robbins J, Bakardjiev AI, Scorrano L. Optic Atrophy 1-Dependent Mitochondrial Remodeling Controls Steroidogenesis in Trophoblasts. *Current Biology*. 2012;22:1228–1234.

42. Sarzi E, Seveno M, Angebault C, Milea D, Rönnbäck C, Quilès M, Adrian M, Grenier J, Caignard A, Lacroux A, Lavergne C, Reynier P, Larsen M, Hamel CP, Delettre C, Lenaers G, Müller A. Increased steroidogenesis promotes early-onset and severe vision loss in females with OPA1 dominant optic atrophy. *Human Molecular Genetics*. 2016;25:2539–2551.

43. Chao de la Barca JM, Fogazza M, Rugolo M, Chupin S, Del Dotto V, Ghelli AM, Carelli V, Simard G, Procaccio V, Bonneau D, Lenaers G, Reynier P, Zanna C. Metabolomics hallmarks OPA1 variants correlating with their in vitro phenotype and predicting clinical severity. *Hum Mol Genet*. 2020;29:1319–1329.

44. Dahl R, Larsen S, Dohlmann TL, Qvortrup K, Helge JW, Dela F, Prats C. Three-dimensional reconstruction of the human skeletal muscle mitochondrial network as a tool to assess mitochondrial content and structural organization. *Acta Physiol (Oxf)*. 2015;213:145–155.

45. Glancy B, Hartnell LM, Malide D, Yu Z-X, Combs CA, Connelly PS, Subramaniam S, Balaban RS. Mitochondrial reticulum for cellular energy distribution in muscle. *Nature*. 2015;523:617–620.

46. Garnier A, Fortin D, Delomenie C, Momken I, Veksler V, Ventura□Clapier R. Depressed mitochondrial transcription factors and oxidative capacity in rat failing cardiac and skeletal muscles. *The Journal of physiology*. 2003;551:491–501.

47. Mukund K, Subramaniam S. Skeletal muscle: A review of molecular structure and function, in health and disease. *Wiley Interdisciplinary Reviews: Systems Biology and Medicine*. 2020;12:e1462.

48. Lin I-H, Chang J-L, Hua K, Huang W-C, Hsu M-T, Chen Y-F. Skeletal muscle in aged mice reveals extensive transformation of muscle gene expression. *BMC genetics*. 2018;19:1–13.

49. Galpin AJ, Raue U, Jemiolo B, Trappe TA, Harber MP, Minchev K, Trappe S. Human skeletal muscle fiber type specific protein content. *Anal Biochem*. 2012;425:175–182.

50. Sanz A, Stefanatos RK. The mitochondrial free radical theory of aging: a critical view. *Current aging science*. 2008;1:10–21.

51. Rolo AP, Palmeira CM. Diabetes and mitochondrial function: role of hyperglycemia and oxidative stress. *Toxicology and applied pharmacology*. 2006;212:167–178.

52. Lavorato M, Iyer VR, Dewight W, Cupo RR, Debattisti V, Gomez L, Fuente SD la, Zhao Y-T, Valdivia HH, Hajnóczky G, Franzini-Armstrong C. Increased mitochondrial nanotunneling activity, induced by calcium imbalance, affects intermitochondrial matrix exchanges. *PNAS*. 2017;114:E849–E858.

53. Liu T, Woo JA, Bukhari MZ, LePochat P, Chacko A, Selenica MB, Yan Y, Kotsiviras P, Buosi SC, Zhao X. CHCHD10□regulated OPA1□mitofilin complex mediates TDP□43□induced mitochondrial phenotypes associated with frontotemporal dementia. *The FASEB Journal*. 2020;34:8493–8509.

54. de La Barca JMC, Arrázola MS, Bocca C, Arnauné-Pelloquin L, Iuliano O, Tcherkez G, Lenaers G, Simard G, Belenguer P, Reynier P. The metabolomic signature of Opa1 deficiency in rat primary cortical neurons shows aspartate/glutamate depletion and phospholipids remodeling. *Scientific reports*. 2019;9:1–8.

55. Bocca C, Nzoughet JK, Leruez S, Amati-Bonneau P, Ferré M, Kane M-S, Veyrat-Durebex C, de La Barca JMC, Chevrollier A, Homedan C. A plasma metabolomic signature involving purine metabolism in human optic atrophy 1 (OPA1)-related disorders. *Investigative ophthalmology & visual science*. 2018;59:185–195.

56. de La Barca JMC, Simard G, Sarzi E, Chaumette T, Rousseau G, Chupin S, Gadras C, Tessier L, Ferré M, Chevrollier A. Targeted metabolomics reveals early dominant optic atrophy signature in optic nerves of Opa1delTTAG/+ mice. *Investigative ophthalmology & visual science*. 2017;58:812–820.

57. Garcia-Cazarin ML, Snider NN, Andrade FH. Mitochondrial isolation from skeletal muscle. *JoVE (Journal of Visualized Experiments)*. 2011;:e2452.

58. Wortel IMN, van der Meer LT, Kilberg MS, van Leeuwen FN. Surviving Stress: Modulation of ATF4-Mediated Stress Responses in Normal and Malignant Cells. *Trends Endocrinol Metab*. 2017;28:794–806.

59. Cristae undergo continuous cycles of membrane remodelling in a MICOS-dependent manner. *EMBO reports*. 2020;21:e49776.

60. Hessenberger M, Zerbes RM, Rampelt H, Kunz S, Xavier AH, Purfürst B, Lilie H, Pfanner N, van der Laan M, Daumke O. Regulated membrane remodeling by Mic60 controls formation of mitochondrial crista junctions. *Nat Commun*. 2017;8:15258.

61. Tarasenko D, Barbot M, Jans DC, Kroppen B, Sadowski B, Heim G, Möbius W, Jakobs S, Meinecke M. The MICOS component Mic60 displays a conserved membrane-bending activity that is necessary for normal cristae morphology. *J Cell Biol*. 2017;216:889–899.

62. Rieusset J. The role of endoplasmic reticulum-mitochondria contact sites in the control of glucose homeostasis: an update. *Cell death & disease*. 2018;9:1–12.

63. Han J, Back SH, Hur J, Lin Y-H, Gildersleeve R, Shan J, Yuan CL, Krokowski D, Wang S, Hatzoglou M. ER-stress-induced transcriptional regulation increases protein synthesis leading to cell death. *Nature cell biology*. 2013;15:481–490.

64. Zhang X, Wang X, Yuan Z, Radford SJ, Liu C, Libutti SK, Zheng XFS. Amino acids-Rab1A-mTORC1 signaling controls whole-body glucose homeostasis. *Cell Reports*. 2021;34:108830.

65. Rampelt H, Wollweber F, Licheva M, de Boer R, Perschil I, Steidle L, Becker T, Bohnert M, van der Klei I, Kraft C, van der Laan M, Pfanner N. Dual role of Mic10 in mitochondrial cristae organization and ATP synthase-linked metabolic adaptation and respiratory growth. *Cell Reports*. 2022;38:110290.

66. Darshi M, Mendiola VL, Mackey MR, Murphy AN, Koller A, Perkins GA, Ellisman MH, Taylor SS. ChChd3, an inner mitochondrial membrane protein, is essential for maintaining crista integrity and mitochondrial function. *Journal of biological chemistry*. 2011;286:2918–2932.

67. Piñero-Martos E, Ortega-Vila B, Pol-Fuster J, Cisneros-Barroso E, Ruiz-Guerra L, Medina-Dols A, Heine-Suñer D, Lladó J, Olmos G, Vives-Bauzà C. Disrupted in schizophrenia 1 (DISC1) is a constituent of the mammalian mitochondrial contact site and cristae organizing system (MICOS) complex, and is essential for oxidative phosphorylation. *Human Molecular Genetics*. 2016;25:4157–4169.

68. Genin EC, Plutino M, Bannwarth S, Villa E, Cisneros□Barroso E, Roy M, Ortega□Vila B, Fragaki K, Lespinasse F, Pinero□Martos E. CHCHD 10 mutations promote loss of

mitochondrial cristae junctions with impaired mitochondrial genome maintenance and inhibition of apoptosis. *EMBO molecular medicine*. 2016;8:58–72.

69. Park Y-U, Jeong J, Lee H, Mun JY, Kim J-H, Lee JS, Nguyen MD, Han SS, Suh P-G, Park SK. Disrupted-in-schizophrenia 1 (DISC1) plays essential roles in mitochondria in collaboration with Mitofilin. *Proceedings of the National Academy of Sciences*. 2010;107:17785–17790.

70. Genin EC, Bannwarth S, Lespinasse F, Ortega-Vila B, Fragaki K, Itoh K, Villa E, Lacas-Gervais S, Jokela M, Auranen M, Ylikallio E, Mauri-Crouzet A, Tyynismaa H, Vihola A, Augé G, Cochaud C, Sesaki H, Ricci J-E, Udd B, Vives-Bauza C, Paquis-Flucklinger V. Loss of MICOS complex integrity and mitochondrial damage, but not TDP-43 mitochondrial localisation, are likely associated with severity of CHCHD10-related diseases. *Neurobiology of Disease*. 2018;119:159–171.

71. Bannwarth S, Ait-El-Mkadem S, Chaussenot A, Genin EC, Lacas-Gervais S, Fragaki K, Berg-Alonso L, Kageyama Y, Serre V, Moore DG, Verschueren A, Rouzier C, Le Ber I, Augé G, Cochaud C, Lespinasse F, N'Guyen K, de Septenville A, Brice A, Yu-Wai-Man P, Sesaki H, Pouget J, Paquis-Flucklinger V. A mitochondrial origin for frontotemporal dementia and amyotrophic lateral sclerosis through CHCHD10 involvement. *Brain*. 2014;137:2329–2345.

72. Eramo MJ, Lisnyak V, Formosa LE, Ryan MT. The 'mitochondrial contact site and cristae organising system' (MICOS) in health and human disease. *The Journal of Biochemistry*. 2020;167:243–255.

73. Martin CR, Preedy VR, Rajendram R. Assessments, Treatments and Modeling in Aging and Neurological Disease: The Neuroscience of Aging. Academic Press; 2021: 1-608.

74. Kandlur A, Satyamoorthy K, Gangadharan G. Oxidative Stress in Cognitive and Epigenetic Aging: A Retrospective Glance. *Frontiers in Molecular Neuroscience*. 2020;13. Available at https://www.frontiersin.org/article/10.3389/fnmol.2020.00041. Accessed March 17, 2022.

75. Boudina S, Sena S, Theobald H, Sheng X, Wright JJ, Hu XX, Aziz S, Johnson JI, Bugger H, Zaha VG, Abel ED. Mitochondrial energetics in the heart in obesity-related diabetes: direct evidence for increased uncoupled respiration and activation of uncoupling proteins. *Diabetes*. 2007;56:2457–2466.

76. Neikirk K, Vue Z, Katti P, Shao J, Christensen TA, Lopez EG, Marshall A, Palavicino-Maggio C, Ponce J, Alghanem A. Systematic Transmission Electron Microscopy-Based Identification of Cellular Degradation Machinery. *bioRxiv*. 2021.

77. Li B, Tang J, Yang Q, Li S, Cui X, Li Y, Chen Y, Xue W, Li X, Zhu F. NOREVA: normalization and evaluation of MS-based metabolomics data. *Nucleic acids research*. 2017;45:W162–W170.

78. Cantor JR, Abu-Remaileh M, Kanarek N, Freinkman E, Gao X, Louissaint Jr A, Lewis CA, Sabatini DM. Physiologic medium rewires cellular metabolism and reveals uric acid as an endogenous inhibitor of UMP synthase. *Cell*. 2017;169:258–272.

79. Chong J, Soufan O, Li C, Caraus I, Li S, Bourque G, Wishart DS, Xia J. MetaboAnalyst 4.0: towards more transparent and integrative metabolomics analysis. *Nucleic acids research*. 2018;46:W486–W494.

80. Phillips MA, Arnold KR, Vue Z, Beasley HK, Garza-Lopez E, Marshall AG, Morton DJ, McReynolds MR, Barter TT, Hinton A. Combining Metabolomics and Experimental Evolution Reveals Key Mechanisms Underlying Longevity Differences in Laboratory Evolved Drosophila melanogaster Populations. *International Journal of Molecular Sciences*. 2022;23:1067.

81. Wende AR, O'Neill BT, Bugger H, Riehle C, Tuinei J, Buchanan J, Tsushima K, Wang L, Caro P, Aili G, Sloan C, Kim BJ, Wang X, Pereira RO, McCrory MA, Nye BG, Benavides GA, Darley-Usmar VM, Shioi T, Weimer BC, Abela ED. Enhanced cardiac Akt/protein kinase B signaling contributes to pathological cardiac hypertrophy in part by impairing mitochondrial function via transcriptional repression of mitochondrion-targeted nuclear genes. *Molecular and Cellular Biology*. 2015;35:831–846.

(13) **SUPPORTING INFORMATION**

(14) TABLES

(15) FIGURE LEGEND

Figure 1: Decreased mitochondrial size and volume in skeletal muscle of aged mice in SBF-SEM 3D reconstructions.
(**A-C**) Representative SBF-SEM orthoslice for skeletal muscle. (**A'-C'**) 3D reconstructions of mitochondria (various colors) in skeletal muscle mouse tissues of different ages overlaid on ortho slices. (**A''-C''**) 3D reconstructed and isolated mitochondria for clear visualization. (**A'-C''**) Pseudo-colored individual mitochondria in skeletal muscle to differentiate micro-level changes. (**A, A', A''**) The 2D ortho slice, the overlay of the 2D ortho slice, and the 3D reconstruction with individually colored mitochondria in tissue from 3-month-old mice. (**B, B', B''**) The 2D ortho slice, the overlay of the 2D ortho slice, and the 3D reconstruction with individually colored mitochondria in tissue from 1-year-old mice. (**C, C', C''**) The 2D ortho slice, the overlay of the 2D ortho slice, and the 3D reconstruction with individually colored mitochondria in tissue from 2-year-old mice. (**D-F**) Quantification of 3D reconstructions. (**D**) Mitochondrial volume in skeletal muscle of different ages. (**E-F**) Mitochondrial area and perimeter in skeletal tissues of different ages. Significance values **** indicates $p \leq 0.0001$, respectively.

Figure 2: SBF-SEM 3D reconstruction in skeletal muscle of aged mice
(**A-C**) 3D reconstruction of individually colored mitochondria from a transverse view for mouse skeletal tissues of different ages. (**A'-C'**) 3D reconstruction of individually colored mitochondria from a longitudinal view in skeletal muscle tissues of different ages. (**D**) MBI for mitochondria in tissues of different ages. (**F**) Sphericity of mitochondria in skeletal muscle of different ages. (**E**) Representative examples of 3D reconstruction of mitochondria in skeletal muscle of different ages organized by volume. Significance values **** indicates $p \leq 0.0001$, respectively.

Figure 3. Mitochondrial nanotunnels in skeletal mouse tissue.
(**A-C**) TEM tracing showing identified nanotunnels across aged cohorts in skeletal mouse tissue. (**D**) Representative examples of 3D reconstruction of nanotunnels in tissues of different ages organized by volume. (**E-H**) Quantification comparing frequency, average nanotunnel amount, nanotunnel length, and diameter of nanotunnels, respectively, across aged cohorts. (**I**) Histogram showing frequency of various nanotunnel lengths for each age group. (**J**) Histogram showing frequency of various nanotunnel diameters for each age group. **, **** indicate $p \leq 0.01$, and $p \leq 0.0001$, respectively.

Figure 4. Transcription of *Opa-1* and MICOS genes in aging mouse muscle.
(**A-D**) Fold changes in the amount of OPA-1 and MICOS gene transcripts in mitochondria of myocytes of 3-month-old, 1-year-old, and 2-year-old mice as measured by RT-qPCR. (**A**) *Opa-1* transcripts. (**B**) *Mitofilin* transcripts. (**C**) *CHCHD3* transcripts. (**D**) *CHCHD6* transcripts. Significance values *, **, ***, **** indicate $p \leq 0.05$, $p \leq 0.01$, $p \leq 0.001$, and $p \leq 0.0001$, respectively.

Figure 5. Knockout of MICOS complex proteins or *Opa-1* in myotubes results in changes in mitochondria, cristae, and oxygen consumption rates.
(**A-C**) Representative images of mitochondria and cristae from myotubes of OPA-1 and *Mitofilin* knockout mice compared to WT. (**P-S**) Representative images of mitochondria and cristae from myotubes of *Opa-1*, *CHCHD3*, and *CHCHD6* knockout mice compared to WT. (**D, T**) Mitochondrial area in myotubes of *Opa-1*, *CHCHD3*, *CHCHD6*, and *Mitofilin* knockout mice compared to WT. (**E, U**) Circularity index, measuring the roundness and symmetry of mitochondria, in myotubes of *Opa-1*, *CHCHD3*, *CHCHD6*, and *Mitofilin* knockout mice compared to WT. (**F, V**) The number of mitochondria in myotubes of *Opa-1*, *CHCHD3*, *CHCHD6*, and *Mitofilin* knockout mice compared to WT. (**W, G**) Quantification of individual cristae in myotubes of *Opa-1*, *CHCHD3*, *CHCHD6*, and *Mitofilin* knockout mice compared to WT. (**H, X**) Cristae scores measuring the uniformity and idealness of cristae in myotubes of *Opa-1*, *CHCHD3*, *CHCHD6*, and *Mitofilin* knockout mice compared to WT. (**I, Y**) Surface area of the average cristae in myotubes of *Opa-1*, *CHCHD3*, *CHCHD6*, and *Mitofilin* knockout mice compared to WT. (**J, Z**) OCR in myotubes of *Opa-1*, *CHCHD3*, *CHCHD6*, and *Mitofilin* knockout mice compared to WT. **(K, AA)** Basal OCR, the net respiration rate once non-mitochondrial respiration has been removed, in myotubes of *Opa-1*, *CHCHD3*, *CHCHD6*, and *Mitofilin* knockout mice compared to WT. (**L, AB**) ATP-linked respiration, shown from intervals 4−7 in the OCR graphs, was determined by the addition of oligomycin (an inhibitor of respiration), thus representing the respiration dependent on ATP, in myotubes of *Opa-1*, *CHCHD3*, *CHCHD6*, and *Mitofilin* knockout mice compared to WT. (**M, AC**) Maximum OCR, represented by the peak from intervals 7−11 once non-mitochondrial respiration was deducted, in myotubes of *Opa-1*, *CHCHD3*, *CHCHD6*, and *Mitofilin* knockout mice compared to WT. (**N, AD**) The reserve capacity, which is represented by the difference between basal OCR and maximum OCR, in myotubes of *Opa-1*, *CHCHD3*, *CHCHD6*, and *Mitofilin* knockout mice compared to WT. (**O, AE**) Proton leak, representing non-phosphorylating electron transfer, in myotubes of *Opa-1*, *CHCHD3*, *CHCHD6*, and *Mitofilin* knockout mice compared to WT.

Significance values *, **, ***, **** indicate $p \leq 0.05$, $p \leq 0.01$, $p \leq 0.001$, and $p \leq 0.0001$, respectively.

Figure 6. Loss of OPA-1 or MICOS complex proteins in myotubes decreases mitochondrial size and length.
(**A-C**) Representative images showing 3D reconstructions of mitochondria in myotubes of *Opa-1* and *Mitofilin* knockout mice compared to WT. (**D**) Mitochondrial 3D length in myotubes of *Opa-1* and *Mitofilin* knockout mice compared to WT. (**E**) Volume of mitochondria in myotubes of *Opa-1* and *Mitofilin* knockout mice compared to WT. (**F-I**) Representative images showing 3D reconstruction of mitochondria in myotubes of *Opa-1***,** *CHCHD3*, and *CHCHD6* knockout mice compared to WT. (**J**) Mitochondrial 3D length in myotubes of *Opa-1***,** *CHCHD3*, and *CHCHD6* knockout mice compared to WT. (**K**) Mitochondrial volume in myotubes of *Opa-1***,** *CHCHD3*, and *CHCHD6* knockout mice compared to WT. Significance value **** indicates $p \leq 0.0001$.

Figure 7. Metabolomics of myotubes lacking components of the MICOS complex. (**A**) Metabolite PCA for myotubes of *Mitofilin* knockout mice compared to control. (**B**) T-test comparing control to *Mitofilin* knockout mice. (**C**) Heatmap showing the relative abundance of ions for control and *Mitofilin* knockout mice. (**D**) Enrichment analysis of metabolites, which links together several similarly functioning metabolites, with the relative abundance for *Mitofilin* knockout mice. (**E**) PCA for *CHCHD6* and *CHCHD3* knockout mice compared to control. (**F**) ANOVA test comparing control to *CHCHD3* and *CHCHD6* knockout mice. (**G**) Heatmap showing the relative abundance of ions for control, *CHCHD3*, and *CHCHD6* knockout mice. (**H**) Enrichment analysis metabolite, which links together several similarly functioning metabolites, with the relative abundance for *CHCHD3* and *CHCHD6* knockout mice.

Supplementary Figure 1: The (**A**) volume (**B**) 3D area, and (**C**) perimeter of the average mitochondria in each of the three individual mice for the age cohorts.

Supplementary Figure 2: The (**A**) mitochondria branching index (MBI) and (**B**) of the average mitochondria in each of the three individual mice for the age cohorts.

Figure 1

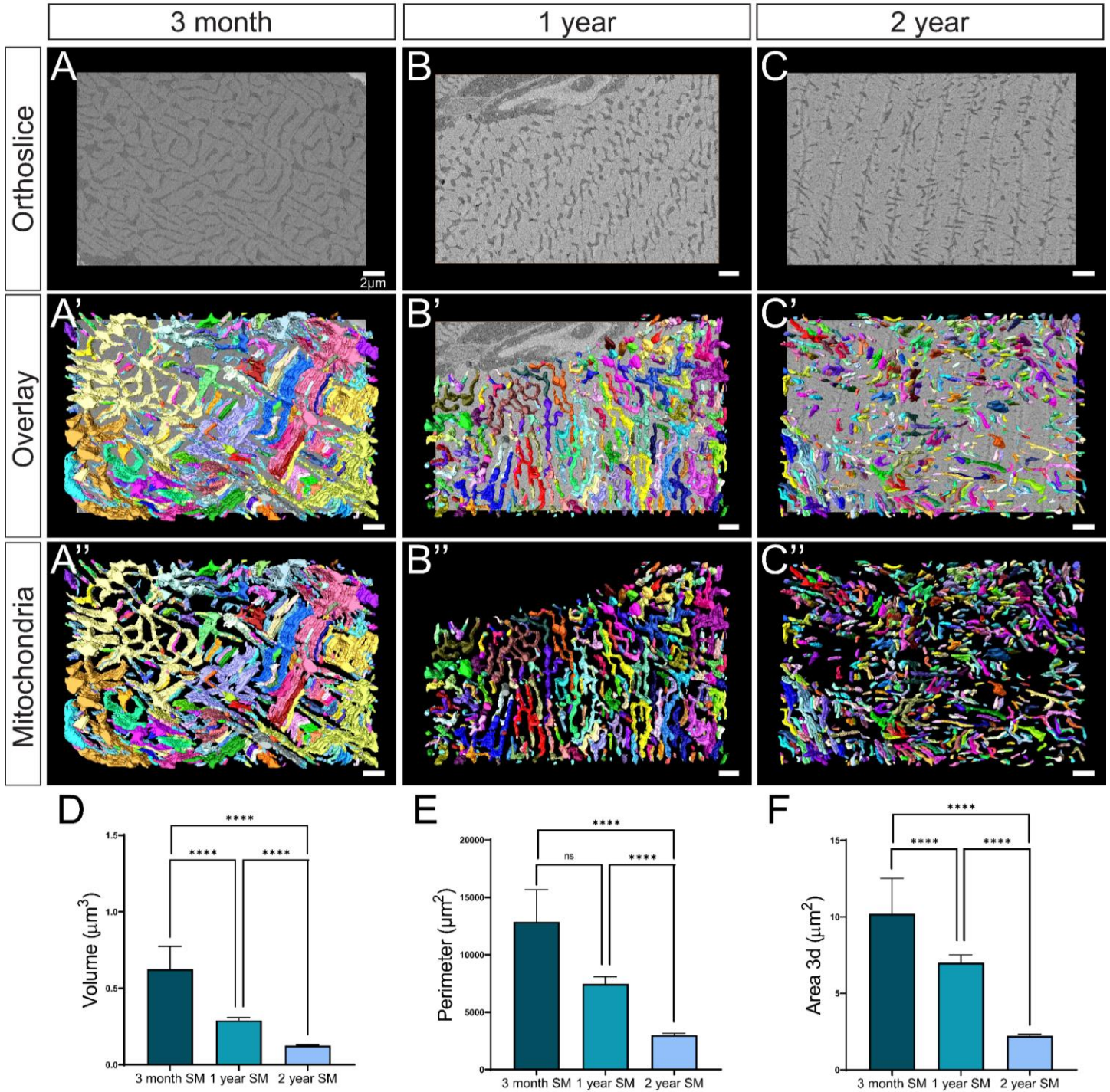
3 month
1 year
2 year
Orthoslice
Overlay
Mitochondria
A
B
C
2µm
A'
B'
C'
A''
B''
C''
D
E
F
Volume (µm3)
Perimeter (µm2)
Area 3d (µm2)
3 month SM
1 year SM
2 year SM
****
ns

Figure 2

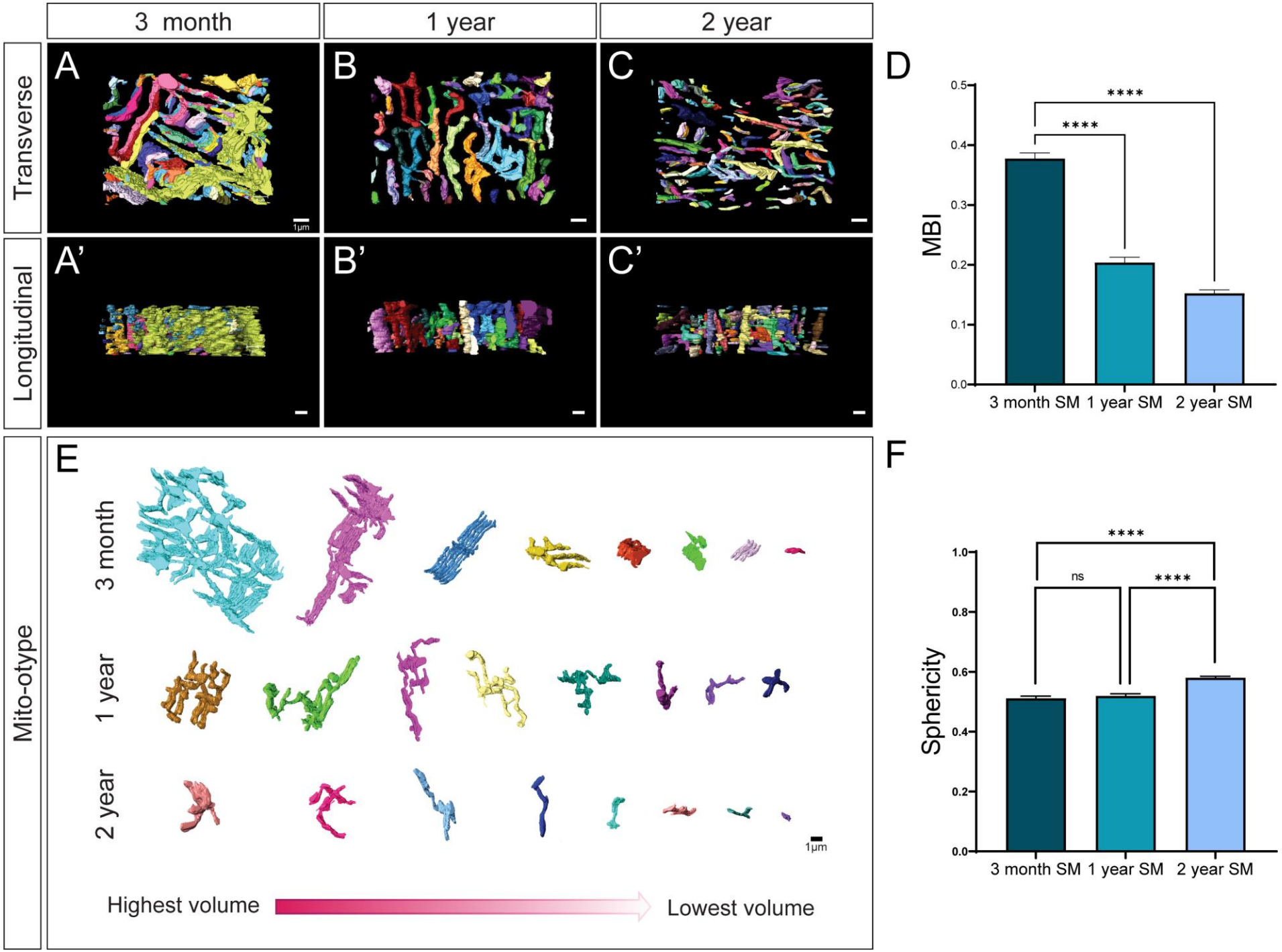
3 month
1 year
2 year
Transverse
Longitudinal
Mito-otype
A
B
C
A'
B'
C'
1µm
D
MBI
0.5
0.4
0.3
0.2
0.1
0.0
****
****
3 month SM
1 year SM
2 year SM
E
3 month
1 year
2 year
1µm
Highest volume
Lowest volume
F
Sphericity
1.0
0.8
0.6
0.4
0.2
0.0
****
ns
****
3 month SM
1 year SM
2 year SM

Figure 3

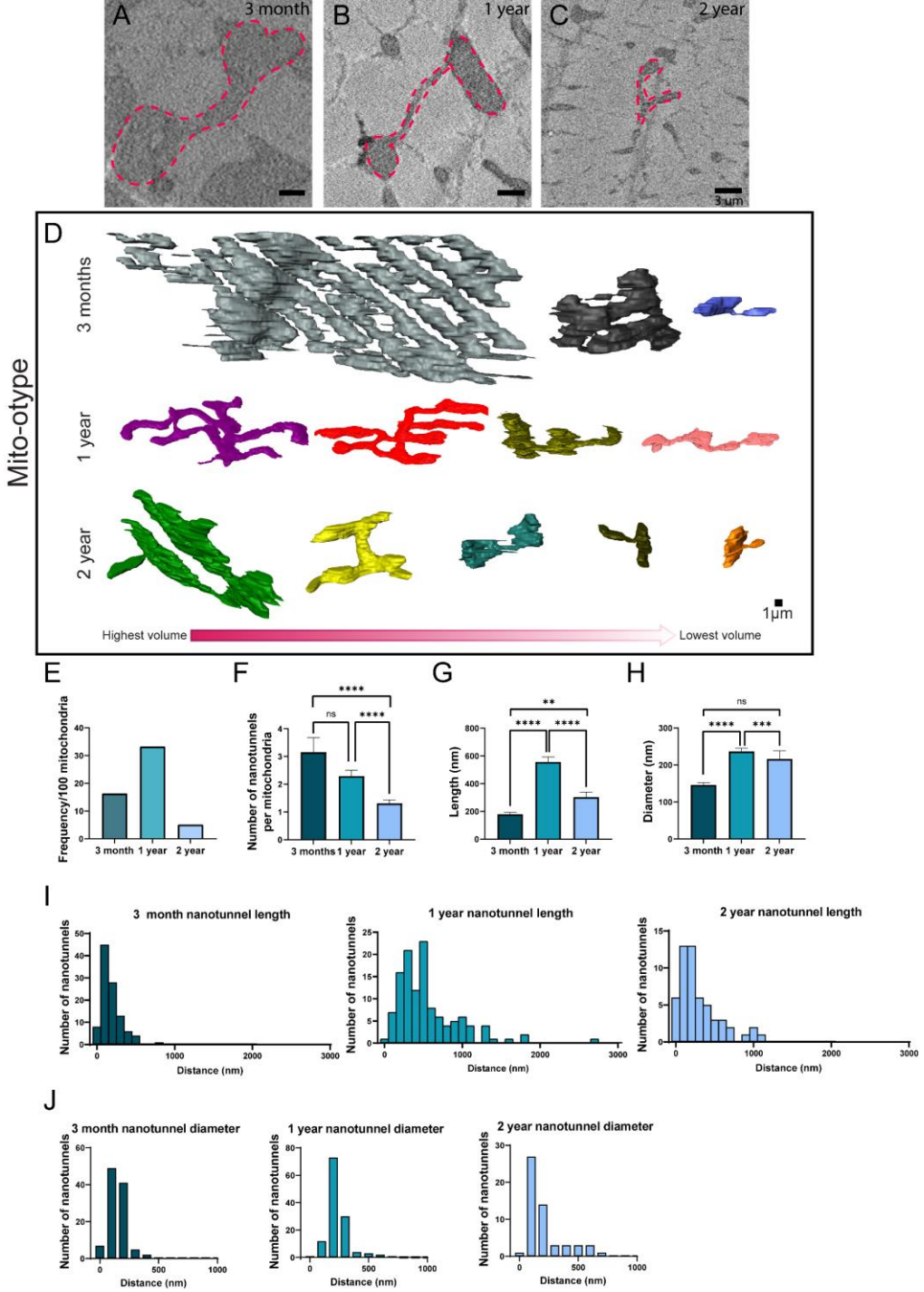
A
3 month
B
1 year
C
2 year
3 µm
D
Mito-otype
3 months
1 year
2 year
1µm
Highest volume
Lowest volume
E
Frequency/100 mitochondria
3 month 1 year 2 year
F
Number of nanotunnels per mitochondria
ns
****
3 months 1 year 2 year
G
Length (nm)
**
****
3 month 1 year 2 year
H
Diameter (nm)
ns
****
***
3 month 1 year 2 year
I
3 month nanotunnel length
1 year nanotunnel length
2 year nanotunnel length
Number of nanotunnels
Distance (nm)
J
3 month nanotunnel diameter
1 year nanotunnel diameter
2 year nanotunnel diameter
Number of nanotunnels
Distance (nm)

Figure 4

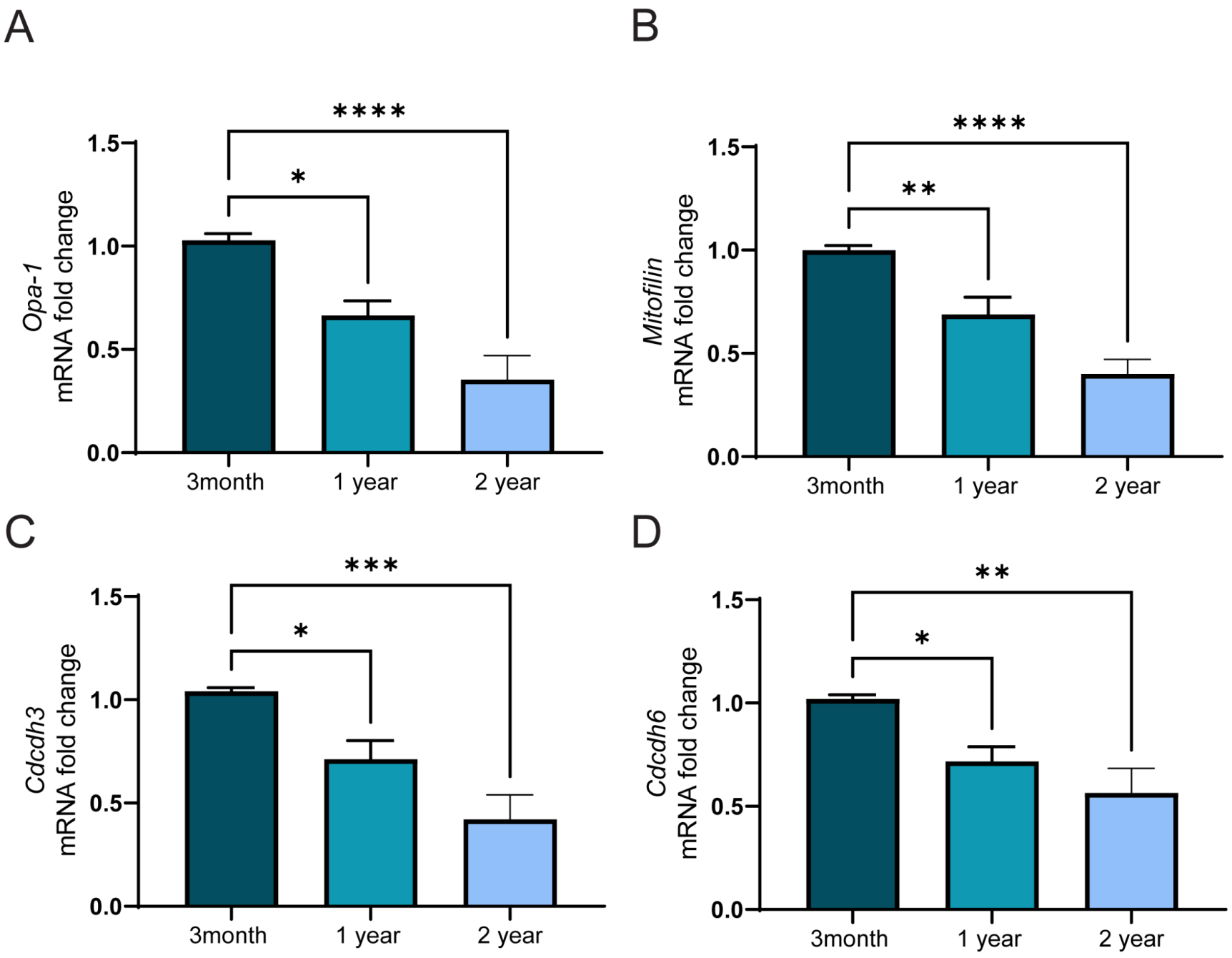
A
****
*
1.5
1.0
0.5
0.0
Opa-1
mRNA fold change
3month
1 year
2 year
B
****
**
1.5
1.0
0.5
0.0
Mitofilin
mRNA fold change
3month
1 year
2 year
C
***
*
1.5
1.0
0.5
0.0
Cdcdh3
mRNA fold change
3month
1 year
2 year
D
**
*
1.5
1.0
0.5
0.0
Cdcdh6
mRNA fold change
3month
1 year
2 year

Figure 5

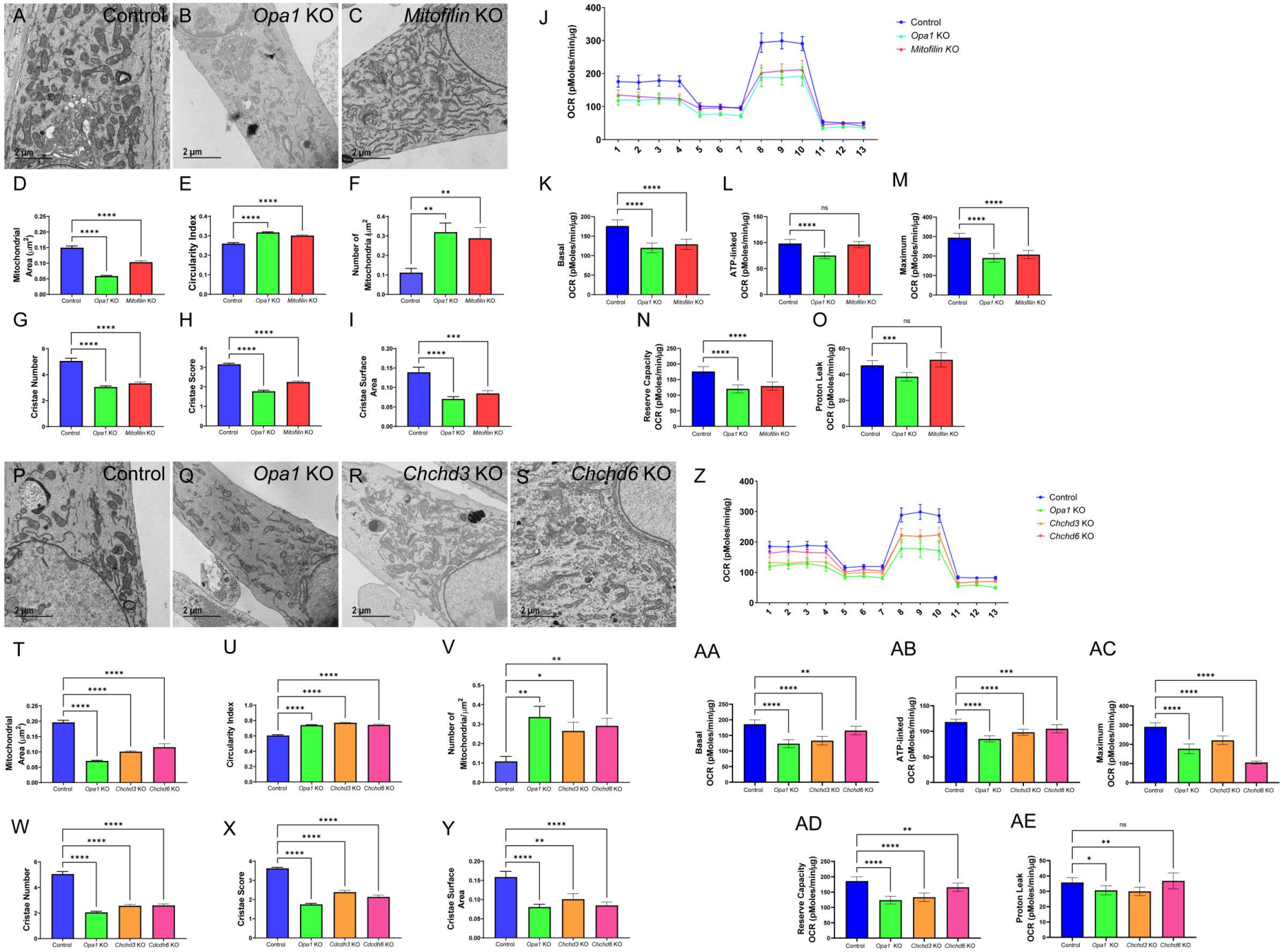
A Control
B Opa1 KO
C Mitofilin KO
2 µm
J
OCR (pMoles/min/µg)
Control
Opa1 KO
Mitofilin KO
D
Mitochondrial Area (µm²)
E
Circularity Index
F
Number of Mitochondria/µm²
K
Basal OCR (pMoles/min/µg)
L
ATP-linked OCR (pMoles/min/µg)
M
Maximum OCR (pMoles/min/µg)
G
Cristae Number
H
Cristae Score
I
Cristae Surface Area
N
Reserve Capacity OCR (pMoles/min/µg)
O
Proton Leak OCR (pMoles/min/µg)
P Control
Q Opa1 KO
R Chchd3 KO
S Chchd6 KO
Z
OCR (pMoles/min/µg)
Control
Opa1 KO
Chchd3 KO
Chchd6 KO
T
U
V
AA
AB
AC
W
X
Y
AD
AE

Figure 6

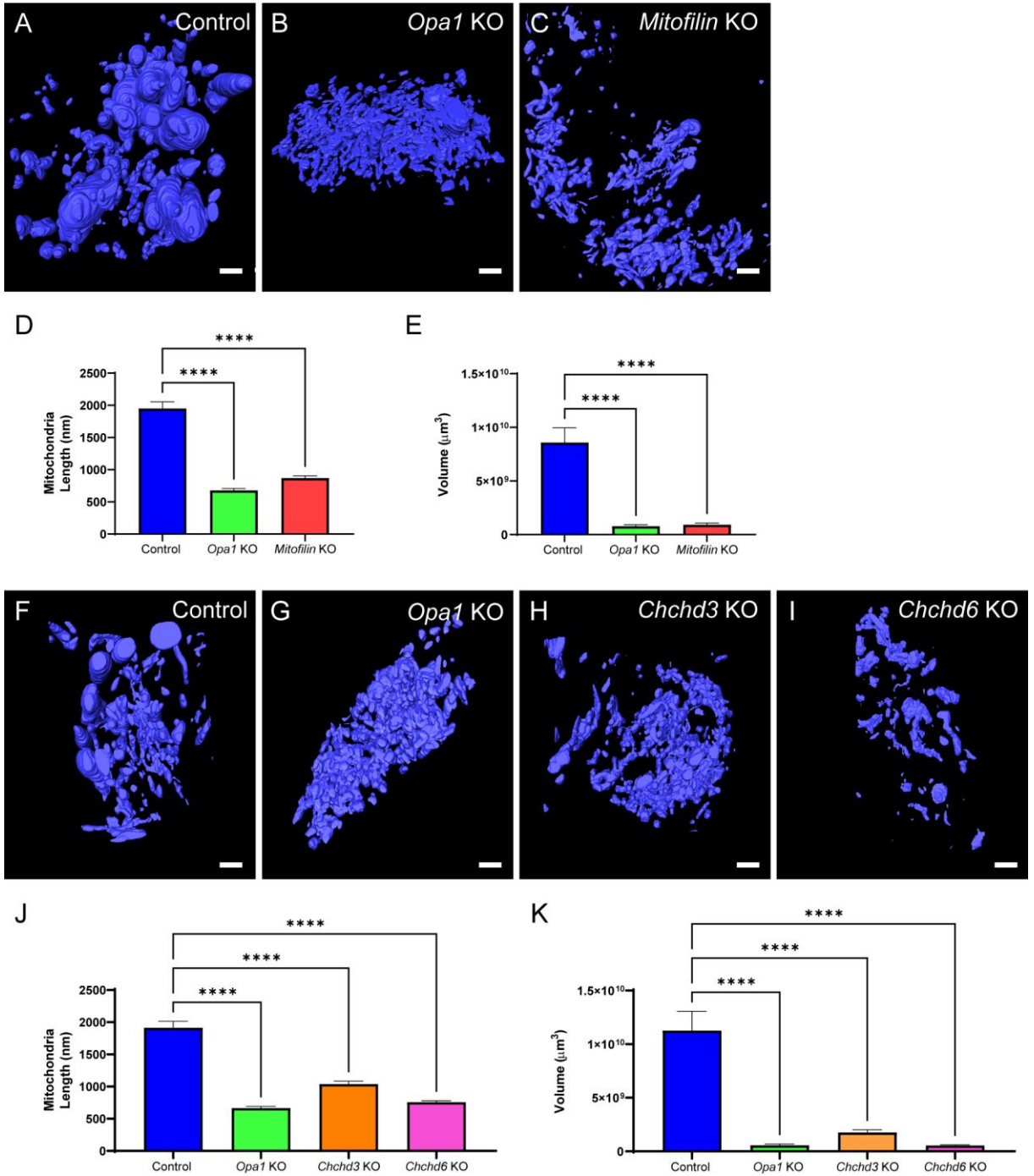
A
Control
B
Opa1 KO
C
Mitofilin KO
D
Mitochondria Length (nm)
2500
2000
1500
1000
500
0
****
****
Control
Opa1 KO
Mitofilin KO
E
Volume (μm³)
1.5×10¹⁰
1×10¹⁰
5×10⁹
0
****
****
Control
Opa1 KO
Mitofilin KO
F
Control
G
Opa1 KO
H
Chchd3 KO
I
Chchd6 KO
J
Mitochondria Length (nm)
2500
2000
1500
1000
500
0
****
****
****
Control
Opa1 KO
Chchd3 KO
Chchd6 KO
K
Volume (μm³)
1.5×10¹⁰
1×10¹⁰
5×10⁹
0
****
****
****
Control
Opa1 KO
Chchd3 KO
Chchd6 KO

Figure 7

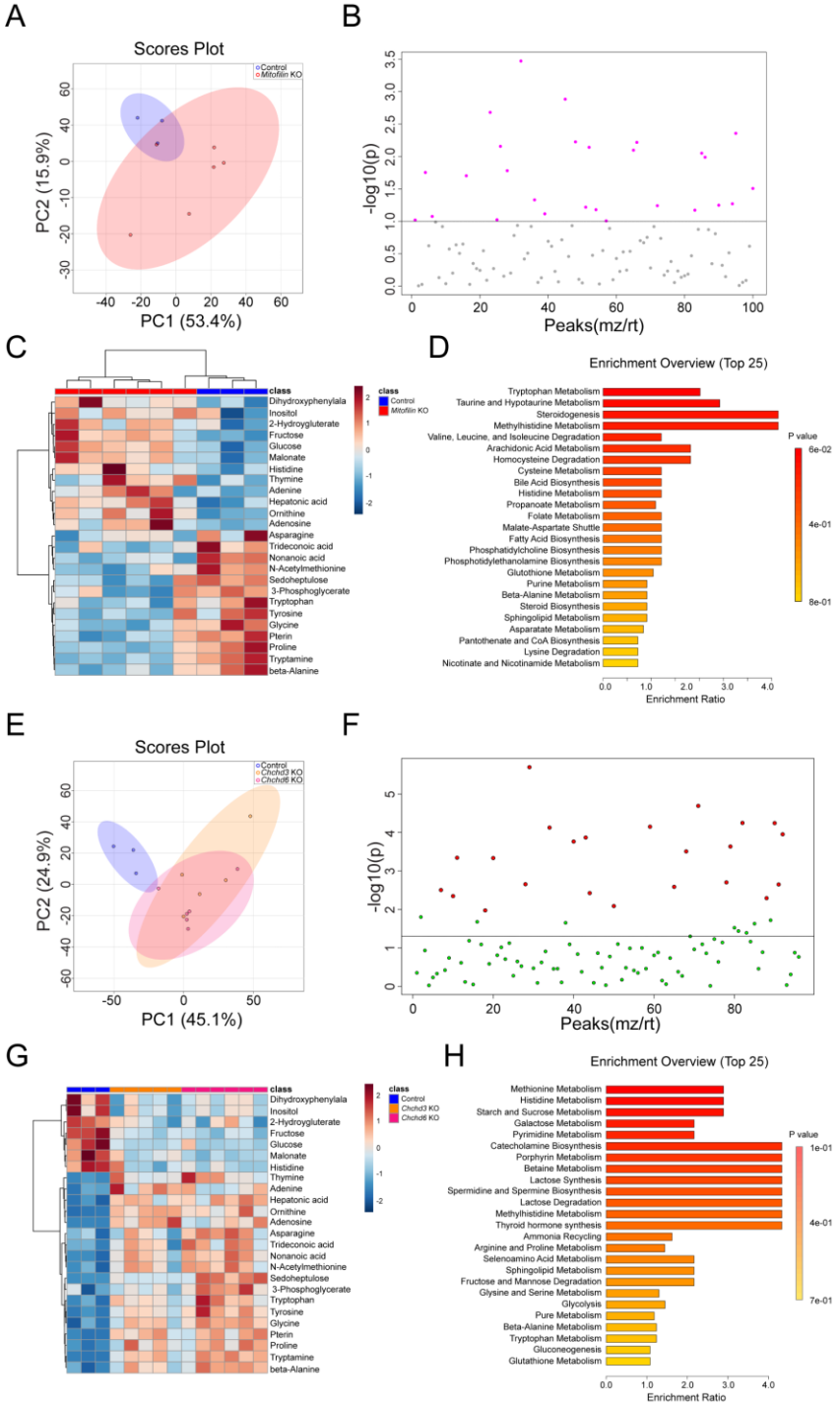
A
Scores Plot
Control
Mitofilin KO
PC2 (15.9%)
PC1 (53.4%)
B
-log10(p)
Peaks(mz/rt)
C
class
Control
Mitofilin KO
Dihydroxyphenylala
Inositol
2-Hydroygluterate
Fructose
Glucose
Malonate
Histidine
Thymine
Adenine
Hepatonic acid
Ornithine
Adenosine
Asparagine
Trideconoic acid
Nonanoic acid
N-Acetylmethionine
Sedoheptulose
3-Phosphoglycerate
Tryptophan
Tyrosine
Glycine
Pterin
Proline
Tryptamine
beta-Alanine
D
Enrichment Overview (Top 25)
Tryptophan Metabolism
Taurine and Hypotaurine Metabolism
Steroidogenesis
Methylhistidine Metabolism
Valine, Leucine, and Isoleucine Degradation
Arachidonic Acid Metabolism
Homocysteine Degradation
Cysteine Metabolism
Bile Acid Biosynthesis
Histidine Metabolism
Propanoate Metabolism
Folate Metabolism
Malate-Aspartate Shuttle
Fatty Acid Biosynthesis
Phosphatidylcholine Biosynthesis
Phosphotidylethanolamine Biosynthesis
Glutothione Metabolism
Purine Metabolism
Beta-Alanine Metabolism
Steroid Biosynthesis
Sphingolipid Metabolism
Asparatate Metabolism
Pantothenate and CoA Biosynthesis
Lysine Degradation
Nicotinate and Nicotinamide Metabolism
P value
6e-02
4e-01
8e-01
Enrichment Ratio
E
Scores Plot
Control
Chchd3 KO
Chchd6 KO
PC2 (24.9%)
PC1 (45.1%)
F
-log10(p)
Peaks(mz/rt)
G
class
Control
Chchd3 KO
Chchd6 KO
Dihydroxyphenylala
Inositol
2-Hydroygluterate
Fructose
Glucose
Malonate
Histidine
Thymine
Adenine
Hepatonic acid
Ornithine
Adenosine
Asparagine
Trideconoic acid
Nonanoic acid
N-Acetylmethionine
Sedoheptulose
3-Phosphoglycerate
Tryptophan
Tyrosine
Glycine
Pterin
Proline
Tryptamine
beta-Alanine
H
Enrichment Overview (Top 25)
Methionine Metabolism
Histidine Metabolism
Starch and Sucrose Metabolism
Galactose Metabolism
Pyrimidine Metabolism
Catecholamine Biosynthesis
Porphyrin Metabolism
Betaine Metabolism
Lactose Synthesis
Spermidine and Spermine Biosynthesis
Lactose Degradation
Methylhistidine Metabolism
Thyroid hormone synthesis
Ammonia Recycling
Arginine and Proline Metabolism
Selenoamino Acid Metabolism
Sphingolipid Metabolism
Fructose and Mannose Degradation
Glysine and Serine Metabolism
Glycolysis
Pure Metabolism
Beta-Alanine Metabolism
Tryptophan Metabolism
Gluconeogenesis
Glutathione Metabolism
P value
1e-01
4e-01
7e-01
Enrichment Ratio